

1 Atmospheric Characterization through Fused Mobile Airborne 2 & Surface *In Situ* Surveys: Methane Emissions Quantification 3 from a Producing Oil Field

4 Ira Leifer¹, Christopher Melton¹, Marc L. Fischer², Matthew Fladeland³, Jason Frash¹, Warren Gore³,
5 Laura Iraci³, Josette Marrero³, Ju-Mee Ryoo³, Tomoaki Tanaka³, Emma Yates³

6 ¹Bubbleology Research International, Solvang, CA 93463, ira.leifer@bubbleology.com

7 ²Lawrence Berkeley National Laboratory, 1 Cyclotron Road, Berkeley CA 94720.

8 ³NASA Ames Research Center, Moffett Field, CA, 94035

9
10 **Correspondence to:** Ira Leifer (Ira.Leifer@bubbleology.com)

11
12 **Abstract.** Methane (CH₄) inventory uncertainties are large, requiring robust emission derivation
13 approaches. We report on a fused airborne/surface data collection approach to derive emissions from an
14 active oil field near Bakersfield, central California. The approach characterizes the atmosphere from the
15 surface to above the Planetary Boundary Layer (PBL) and combines downwind trace gas concentration
16 anomaly (plume) above background with normal winds to derive flux. This approach does not require a
17 well-mixed PBL, allows explicit, data based, uncertainty evaluation, and was applied to complex
18 topography and wind flows.

19
20 *In situ* airborne (collected by AJAX – the Alpha Jet Atmospheric eXperiment) and mobile surface
21 (collected by AMOG – the AutoMOBILE trace Gas – Surveyor) data were collected on 19 August 2015 to
22 assess source strength. Data included an AMOG and AJAX intercomparison transect profiling from the
23 San Joaquin Valley (SJV) floor into the Sierra Nevada Mountains (0.1-2.2 km altitude), validating a novel
24 surface approach for atmospheric profiling by leveraging topography. The profile intercomparison found
25 good agreement in multiple parameters for the overlapping altitude range from 500 to 1500 m, for the
26 upper 5% of surface winds, which accounts for wind-impeding structures, i.e., terrain, trees, buildings,
27 etc. Annualized emissions from the active oil fields were 31.3±16 Gg methane and 2.4±1.2 Tg carbon
28 dioxide. Data showed the PBL was not well-mixed at distances of 10-20 km downwind, highlighting the
29 importance of the experimental design.

31 1. Introduction

32 1.1. Methane Trends and Uncertainty

33 On decadal timescales, methane (CH₄), affects the atmospheric radiative balance more strongly than
34 carbon dioxide (CO₂), (IPCC, 2007, Fig. 2.21). Since pre-industrial times, CH₄ emissions have risen by a
35 factor of 2.5 (Dlugokencky et al., 2011; Khalil and Rasmussen, 1995), while estimates of its lifetime has
36 decreased and now is estimated at ~8.5 years (Sonnemann and Grygalashvily, 2014). Atmospheric CH₄
37 growth almost ceased between 1999 and 2006, but has resumed since 2007 (Nisbet et al., 2014;
38 Schwietzke et al., 2016). Several processes are proposed to underlie this trend (Ghosh et al., 2015; John et
39 al., 2012) with recent isotopic shifts suggesting wetlands are the dominant driver (Nisbet et al., 2016);
40 however, high uncertainty in emission inventories (IPCC, 2013) complicates interpretation of the
41 underlying mechanism(s).

42
43 The dominant CH₄ loss arises from reaction with hydroxyl (OH), whose concentration has been
44 increasing in recent decades (John et al., 2012), causing a decrease in the estimated CH₄ lifetime of 0.5%
45 yr⁻¹ (Karlsdóttir and Isaksen, 2000). Overall, the estimate of the CH₄ lifetime has decreased by ~40% from
46 an estimated 12 years in 2007 (IPCC, 2007). Rigby et al. (2017) suggest a decline in OH is likely to have
47 contributed to increasing CH₄ since 2007. The recent discovery of a new significant CH₄ loss mechanism,
48 terrestrial uptake (Fernandez-Cortes et al., 2015), illustrates the need to understand loss mechanisms
49 better (Allen, 2016).

50
51 Large CH₄ budget uncertainties remain for many sources (IPCC, 2013) with greater uncertainty in future
52 trends from global warming feedback (Rigby et al., 2008) and increasing anthropogenic activities
53 (Kirschke et al., 2013; Saunio et al., 2016; Wunch et al., 2009). Emphasizing these uncertainties are
54 recent studies that suggest underestimation by a factor of 1.5 in the important anthropogenic CH₄ source,
55 Fossil Fuel Industrial (FFI) emissions (Brandt et al., 2014). Tellingly, this discrepancy only was noted
56 recently (Miller et al., 2013), in part because the US CH₄ monitoring network is too sparse to constrain
57 emissions at “regional to national scales” (Dlugokencky et al., 2013). Furthermore, isotopic data indicate
58 even larger underestimation by a factor of 1.6-2.1 (Schwietzke et al., 2016). FFI emissions are the largest
59 (Brandt et al., 2014; EPA, 2017) or second largest after agriculture (Saunio et al., 2016) anthropogenic
60 contributor to the global CH₄ budget. These uncertainties strongly argue for the need for new, robust
61 methodologies for flux derivation.

62 1.2. Methane Flux Estimation

63 Various approaches have been developed to derive surface emissions from CH₄ concentration
64 measurements including direct flux assessment – i.e., measurement of winds and concentrations through a
65 plane, and/or by the comparison of upwind and downwind mass budgets (Peischl et al., 2016; Peischl et
66 al., 2015; White et al., 1976), data-driven mass balance, e.g., Karion et al. (2013), tracer-tracer ratio
67 (LaFranchi et al., 2013), and assimilation inverse models, e.g. Jeong et al. (2013); Jeong et al. (2012);
68 (Saunois et al., 2017). Challenges for the latter approach include the needs for accurate meteorological
69 transport models and good *a priori* emission distributions (Miller et al., 2013; Peischl et al., 2016; Smith
70 et al., 2015). Miller et al. (2013) concluded that bottom-up inventories (EPA, 2013; European
71 Commission, 2010) significantly underestimate husbandry and FFI emissions. To apportion CH₄ to FFI
72 versus biological sources, the tracer-tracer approach has been applied using ethane, whose emission ratio
73 to CH₄ requires tight constraint (Peischl et al., 2013; Simpson et al., 2012; Wennberg et al., 2012). In
74 practice, this emission ratio is an *a priori* assumption in the assessment.

75
76 Direct assessment approaches have advantages over inversion approaches. Direct approaches allow
77 explicit uncertainty evaluation and do not require an *a priori* emission spatial distribution, which may be
78 unknown. Direct approaches also do not require the ability to model atmospheric transport accurately
79 across the study region. In areas of complex topography or highly variable winds, this transport can
80 challenge assimilation approaches, which also are challenged in areas with poorly characterized (or
81 unknown) or highly variable sources, particularly if the measurement network is sparse. For direct
82 assessment approaches, data collection should be rapid if winds and/or emissions are variable, and at
83 adequate data density to characterize fine-scale structure.

84 1.3. Study Motivation

85 Herein we report on a novel application of fused airborne and surface *in situ* data to directly estimate CH₄
86 emissions using an anomaly approach rather than a more typical mass balance approach due to a lateral
87 gradient in the upwind data. A direct approach does not require accurate winds over the study domain,
88 only in the measurement plane. The approach was applied to 1164 km of airborne data collected on 19
89 August 2015 by NASA's Alpha Jet Atmospheric eXperiment (AJAX) while AMOG (AutoMOBILE
90 greenhouse Gas) Surveyor collected 1074 km of contemporaneous mobile surface data. Both platforms
91 measure carbon dioxide (CO₂), CH₄, water vapor (H₂O), and ozone (O₃), as well as winds, pressure,
92 relative humidity (*RH*), and temperature (*T*). The surface and airborne datasets were collected in a

93 downwind curtain or plane oriented approximately orthogonal to the winds, to characterize the full
94 planetary boundary layer (PBL) from surface to above the PBL.

95

96 Additionally, the surface survey route was designed to include an ascent to ~2.2 km above sea level to
97 allow PBL characterization. Data fusion between measurement platforms was validated by a vertical
98 profile intercomparison for 0.5 to 1.5 km altitude by AMOG Surveyor leveraging topographic relief.

99 **1.4 The South San Joaquin Valley, California**

100 Most California oil production lies in the San Joaquin Valley (SJV), as does most of California
101 agriculture, including many intensive dairies (Gentner et al., 2014), and major north-south transportation
102 arteries. For this study, data were collected for the Kern River oil fields (Kern Front oil field, Kern River
103 oil field and the Poso Creek oil field, referred to herein as the Kern Fields), located adjacent to northwest
104 Bakersfield (**Fig. 1A**). These adjacent oil fields create a strong CH₄ source that largely is isolated from
105 confounding plumes from other SJV sources. This area includes complex wind flow patterns across and
106 around the “toe” of Sierra Nevada Mountain foothills, which extend into the Kern Front and Kern River
107 oil fields. Here, topographic steering ensures predictable prevailing northwesterly winds blow across the
108 Kern Fields.

109

110 Strong orographic forcing also arises from tall bluffs (~100 m) on the Kern River Valley’s south bank,
111 which separates the Kern River oil field from the urban city of Bakersfield (pop. 364,000 in 2013). The
112 fine-scale wind structure that results from orographic forcing on transport dictated an anomaly approach
113 for flux derivation, as did the presence of strong CH₄ structures (plumes) in the valley’s lowest air. In the
114 anomaly approach, transects must extend beyond a reasonably well-defined plume.

115

116 Topography (i.e., mountain ranges) plays a locally dominant role in overall southern California air flows
117 where upper level winds locally force the lower level flows that transport pollutants (Bao et al., 2008).
118 The SJV is delimited on the east by the Sierra Nevada Mountains and on the west by the Transverse
119 Coastal Mountain Range (**Fig. 1A**). Transport between the SJV and adjacent air basins is poor due to
120 California’s mountain ranges. The SJV features weak surface winds (Bao et al., 2008) with the worst air
121 quality in the United States occurring in the cities of Bakersfield and Delano (American Lung
122 Association, 2016) in the SJV.

123

124 Pacific Ocean air primarily enters the SJV through the San Francisco Bay area and the Carquinez Strait,
125 where it splits north into the Sacramento Valley and south into the SJV (Zhong et al., 2004). This flow

126 extends up to ~1 km altitude (Zhong et al., 2004). These winds are near orthogonal to the 600-km long
127 central valley of California - i.e., cross-slope. South of Bakersfield, winds shift to from the west due to
128 mountains that guide SJV air out into the Mojave Desert, where it affects air quality for up to hundreds of
129 kilometers distant (VanCuren, 2015). Although the Tehachapi Pass is the main exit pathway of SJV air,
130 other passes also transport air into the Mojave Desert. These flows are augmented by high inland
131 temperatures relative to the Pacific Ocean, which creates a horizontal pressure gradient that drives local
132 upslope flows during the day and returning downslope nocturnal flows (Zhong et al., 2004). The pressure
133 gradient is maximal around sunset, although winds peak ~4 hours later, shortly before midnight. This
134 pressure gradient is controlled by the semi-permanent Pacific high, situated offshore central California,
135 which diverts storms far to the north during summer. This pressure feature drives prevailing west-
136 southwesterly winds at the regional scale in the California south coast air basins (Boucouvala and
137 Bornstein, 2003).

138

139 **2. Methodology**

140 **2.1. Experimental design**

141 Data were collected as part of the *GOSAT-COMEX Experiment* (Greenhouse gases Observing SATellite -
142 CO₂ and Methane Experiment - GCE) Campaign. GCE was developed to characterize emissions on
143 spatial scales from decameter (*in situ* surface, imaging spectroscopy) to kilometer (*in situ* airborne) to
144 deca-kilometer (satellite) in an area of complex topography. GCE design combined *in situ* mobile surface
145 and airborne data with GOSAT satellite data. *In situ* data serve to assess the satellite pixel / plume
146 overlap. Key GCE requirements are relatively steady, strong, isolated emissions and predictable and
147 steady winds. Prevailing study area winds are from the west-northwest, veering to westerly winds to the
148 southeast of Bakersfield (**Fig. 1**). Prevailing wind directions are highly reliable due to topographic
149 control.

150

151 FIGURE 1 HERE

152

153 GCE developed from the COMEX Campaign (Krautwurst et al., 2016), which combined *in situ* airborne
154 and surface observations with both imaging and non-imaging spectroscopy to explore synergies for GHG
155 emission estimation (Thompson et al., 2015). COMEX focused on southern California CH₄ sources
156 including husbandry, landfills, natural geology, and petroleum hydrocarbon refining and production.

157
158 GCE combines airborne and surface data collected at dramatically different speeds. AJAX collects data at
159 $\sim 500 \text{ km hr}^{-1}$, capturing a snapshot of atmospheric winds and plume structure. Surface GCE data are
160 collected quasi-Lagrangian, starting northwest (upwind) and proceeding southeast and then east
161 (downwind). This enables useful data collection even when a CH_4 plume drifts into the study area after
162 the upwind survey – data collection proceeds downwind faster than advection. The surface route was
163 designed carefully to traverse all targeted GOSAT pixels using rarely used (low traffic) surface roads and
164 requires ~ 100 minutes.

165
166 Airborne and surface surveys are timed so that the downwind data plane (Krings et al., 2011) is surveyed
167 concurrent with the satellite overpass. Data planes extend from the surface (AMOG) to above the PBL
168 (AJAX), reducing uncertainty by providing a more complete atmospheric characterization including
169 below where airplanes are permitted to fly ($\sim 500 \text{ m}$ in an urban area). AJAX and AMOG profile data are
170 fused by an interpolation approach that imposes the observed vertical structure and the flux through the
171 data curtain is calculated (Sect. 2.5).

172
173 GCE first incorporates an AMOG Surveyor upwind transit from Delano (100 m) on the SJV floor to
174 Sierra Alta (1800 m) and higher to confirm that upwind CH_4 plumes do not threaten to impact the study
175 area during the experiment, otherwise the survey is aborted. A key mission abort criterion is wind
176 compliance. Specifically, winds must not be too light (typically less than $\sim 2 \text{ m s}^{-1}$) or variable ($>30^\circ$), and
177 must flush nocturnal accumulations before the GOSAT overpass (i.e., no CH_4 cloud at or nearby upwind
178 of the site. This means that winds cannot be light as recently as several hours prior and must be
179 prevailing. The upwind transit provides vertical profile information including PBL height and vertical
180 structure. AJAX repeats this upwind transect to compare wind profiles with AMOG; however,
181 discrepancies in the transects arise from the road following terrain, and the airplane needing to avoid
182 peaks along the ridge.

183 **2.2. AutoMOBILE trace Gas (AMOG) Surveyor**

184 Mobile atmospheric surface measurements have been conducted for many years using a customized van
185 (Lamb et al., 1995) or a recreational vehicle (Farrell et al., 2013; Leifer et al., 2013). Recently, the
186 development of cavity enhanced absorption spectroscopy (CEAS) analyzers has opened the way for rapid
187 and highly accurate trace gas measurements (Leen et al., 2013) without the need for onboard compressed
188 gases as in gas chromatography (Farrell et al., 2013), although periodic calibration with gas standards is
189 important, albeit typically not onboard the platform. This allows for smaller vehicle survey platforms at

190 lower logistical overhead (Leifer et al., 2014; McKain et al., 2015; Pétron et al., 2012; Yacovitch et al.,
191 2015). A competing sensor technology that has been used in mobile survey data collection is open path
192 spectroscopy (Sun et al., 2014). Mobile survey platforms can incorporate older technology such as
193 fluorescence to, for example, measure ozone, O₃.

194
195 Mobile surface data were collected by AMOG Surveyor (Leifer et al., 2014), a modified commuter car
196 (see Supp. Sect. S2.1 for additional details). AMOG Surveyor provides mobile high-speed, high-spatial
197 resolution observations of meteorology (winds, temperature, pressure), trace gases (greenhouse and
198 others), and remote sensing parameters. AMOG Surveyor uses a range of trace gas analyzers and careful
199 design with respect to wind flow around the vehicle to characterize strong spatial heterogeneity at up to
200 highway speeds.

201
202 Two-dimensional winds are measured by a sonic anemometer (VMT700, Vaisala) mounted 1.4 m above
203 the roof, at 3.0 m above the surface, and above vehicle flow streamlines for slow to highway speeds.
204 Estimated accuracy is approximately 10° and 0.3 m s⁻¹ for wind speeds above 1.5 m s⁻¹ (see supplement
205 for further details).

206
207 A high-flow vacuum pump (GVB30, Edwards Vacuum) draws air down a sample lines from 5 and 3 m
208 above ground for GHG and ozone (O₃) analyzers. The 5-m sample line height references low speed /
209 stopped (< a few m s⁻¹) AMOG sample collection. At high speed (> 10 m s⁻¹) the sample tube flexes
210 backwards to 3 m height to avoid destructively hitting obstacles at high speed. This protects the sample
211 line from hitting bridges, tree branches, etc. Greenhouse gases, CO₂, CH₄, and H₂O, are measured at up to
212 10 Hz by an Integrated Cavity Offaxis Spectrometer-Cavity Enhanced Absorption Spectroscopy analyzer,
213 with a 1 s accuracy of 1 ppb for CH₄ (ICOS-CEAS, 911-0010, Los Gatos Research, Inc.). Calibration is
214 with a Scott-Marine CH₄ and CO₂ atmospheric standard. A fluorescence analyzer measured O₃ at 0.25 Hz
215 (49C, ThermoFischer Scientific, MA). This difference does not arise from calibration differences; the
216 AMOG Surveyor O₃ analyzer was cross calibrated with the AJAX calibration source to 1 ppb accuracy.
217 AMOG Surveyor's full trace gas suite (carbonyl sulfide, carbon monoxide, nitric oxide, nitrogen dioxide,
218 hydrogen sulfide, sulfur dioxide, total sulfur, ammonia) was not deployed on 19 Aug. 2015.

219
220 FIGURE 2

221
222 The greenhouse gas analyzer is calibrated using a Scotty's whole-air standard before and/or after each
223 data collection with the calibration factor closest to the day of flight being applied to each raw CO₂ and

224 CH₄ measurement. Calibration factors have been shown to agree within less than 1 ppb. The calibration
225 factor includes a linear correction for cell pressure, which can drop at higher altitudes. This pressure
226 calibration has been shown to be linear from 140 mtorr down to 28 mtorr.

227
228 Relevant recent AMOG Surveyor improvements since Leifer et al. (2014) include a high speed
229 thermocouple (50416-T, Cooper-Atkins) and a high accuracy (0.2 hPa) pressure sensor (61320V RM
230 Young Co.). Both are mounted in a roof passive radiation shield (7710, Davis Instruments) to largely
231 eliminate dynamic pressure effects from the airflow. Position information is critical to accurate wind
232 measurements and is provided by redundant (two) Global Navigation Satellite Systems (19X HVS,
233 Garmin) that use the GLONASS, GPS, Galileo, and QZSS satellites at 10 Hz (WGS84). AMOG
234 Surveyors' analyzers' and sensor data are logged asynchronously on a single computer. Custom software
235 integrates the data streams and provides real-time visualization of multiple parameters in the Google
236 Earth environment.

237 **2.3. Alpha Jet Atmospheric eXperiment (AJAX)**

238 AJAX (Fig. 2b) collected airborne *in situ* measurements of CO₂, CH₄, H₂O by cavity ring down
239 spectroscopy (G2301-m, Picarro Inc.), O₃, (Model 205, 2B Technologies Inc.), and meteorological
240 parameters including 3D winds by the Meteorological Measurement System
241 (<https://earthscience.arc.nasa.gov/mms>), a NASA developed system with accuracy of $\pm 1 \text{ m s}^{-1}$. The
242 greenhouse gas analyzer is calibrated using NOAA whole-air standards; calibrations are performed before
243 and/or after each flight with the calibration factor closest to the day of flight being applied to each raw
244 CO₂ and CH₄ measurement. Further corrections include applying water vapor corrections provided by
245 Chen et al. (2010) to calculate CO₂ and CH₄ dry mixing ratios. Data are quality control filtered for
246 deviations in instrument cavity pressure, to improve inflight precision.

247
248 Overall CH₄ measurement uncertainty is typically <2.2 ppb, including contributions from accuracy of the
249 standard, precision (1- σ over 6 min), calibration repeatability, inflight variance due to cavity pressure
250 fluctuations, and uncertainty due to water corrections and pressure dependence (based on environmental
251 chamber studies). See Hamill et al. (2015); Tanaka et al. (2016), and Yates et al. (2013) for further
252 aircraft and instrumentation details, and Supp. Sect. S2.2.

253 **2.4. Background estimation and data fusion**

254 The flux ($Q(x, z)$) in moles $s^{-1} m^{-2}$ with respect to lateral transect distance (x) and altitude (z) through the
 255 x, z plane is the product of the normal winds ($U_N(x, z)$) in $m s^{-1}$ and the plume concentration anomaly
 256 ($C'(x, z)$) or mole fraction in ppm (Leifer et al., 2016).

$$257 \quad Q(x, z) = k(z) U_N(x, z) C'(x, z) = k(z) U_N(x, z) (C(x, z) - C_B(x, z)) \quad (1)$$

258 $k(z)$ converts from ppm to moles. Interpolation of C' and U_N is linear within the PBL and is assumed
 259 uniform above the PBL. To calculate $Q(x, z)$ requires C' relative to background ($C_B(x, z)$). Initially surface
 260 data that was collected for an upwind surface transect was used to derive C_B , using the assumption of
 261 vertical uniformity for “background.”

262

263 Unfortunately, the upwind data showed a lateral gradient, which coupled with uncertainty in precisely
 264 where the downwind air originated (given the topography, which features a gentle incline towards the
 265 northeast, this gradient is unsurprising, in retrospect). Thus a very small shift in the winds between the
 266 upwind and downwind curtains results in a significant shift in C_B , with a very large effect on Q . As a
 267 result, the more traditional upwind/downwind mass balance approach was abandoned for an anomaly
 268 approach.

269

270 In the anomaly approach, $C_B(x, z)$ was derived from evaluating $C_B(x < x_{max}/2, z)$ and $C_B(x > x_{max}/2, z)$,
 271 denoted $C_{BL}(z)$ and $C_{BR}(z)$, respectively, where x_{max} is the lateral extent of the data curtain. Then, $C_B(x, z)$ is
 272 derived from a first order linear polynomial fit of $C_{BL}(z)$ and $C_{BR}(z)$.

273

274 Both $C_{BL}(z)$ and $C_{BR}(z)$ are derived from the amplitude of a Gaussian fit to the left and right probability
 275 density functions ($\Phi_L(C(x < x_{max}/2, z))$ and ($\Phi_R(C(x > x_{max}/2, z))$), respectively, for each flight transect level.
 276 Specifically, for Φ_L and Φ_R , Gaussian functions are fit to model the plume distribution (Φ_P) and the
 277 background distribution (Φ_B). In these data, Φ_B is well-fit by a single Gaussian, while Φ_P is best described
 278 by multiple Gaussian functions. Then, $C_{BL}(z)$ and $C_{BR}(z)$ are defined such that,

$$279 \quad \int \Phi_{BL}(C_{BL}(z)) = 0 \text{ and } \int \Phi_{BR}(C_{BR}(z)) = 0. \quad (2)$$

280 where Φ_{BL} and Φ_{BR} are the background Φ_B for the left and right halves of the data plane, respectively.

281 Concentration is not a conserved value, thus C' is converted into mass (N') by the ideal gas law (k in Eq
 282 1) for spatial integration to derive the total emissions (E), which is the integration of the flux through the
 283 plane, Q ,

284
$$E = \int_{x_1}^{x_2} \int_0^{z=PBL} Q(x, z) dz dx \quad (3)$$

285 Interpolation, prior to integration, is linear.

286 **2.5. Uncertainty evaluation for emission calculation**

287 The flux calculation has two source of uncertainty: accuracy and representativeness. Specifically,
288 background concentration profiles may be incorrect, while winds, which are measured accurately, could
289 be un-representative, as could concentrations due to temporal variability over the period needed to make
290 the measurements. Monte Carlo simulations based on observed data variability were run to assess
291 uncertainty. Instrumental accuracy uncertainty is far less than spatial and temporal variability. Thus,
292 spatial and temporal variability are the dominant source of uncertainty (Leifer et al., 2016).

293
294 Monte Carlo simulations were based on 1 standard deviation in the observed $U_N(z)$ around the mean for
295 each flight transect altitude level on the right and left sides, i.e., $U_{N_L}(z)$ and $U_{N_R}(z)$. Gaussian
296 distributions with half-widths of 1σ based on the values of $U_{N_L}(x,z)$ and $U_{N_R}(x,z)$ was formed for each
297 transect altitude. The distribution was randomly sampled to populate $U_N(x,z)$, and then interpolated as
298 described above. Other variables were Monte Carlo simulated in the same manner, i.e., a Gaussian
299 distribution was calculated for the left and right portions of the data based on 1 standard deviation in the
300 observations of the variable around its mean. Variables then were randomly sampled and interpolated.
301 Specifically, Monte Carlo simulations also addressed C_B , and C . Because instrumentation error is so much
302 less than spatial and temporal variability, Monte Carlo simulation of C_B represents uncertainty in the
303 source of the background (upwind) air, which could have some veering from the east or west coupled
304 with convergence in the horizontal plane. One million Monte Carlo simulations were run for a flux
305 uncertainty calculation.

306 **3. Results**

307 **3.1. Profile data**

308 Four vertical profiles (surface and airborne) were collected to understand PBL evolution during the
309 survey (2 hrs.) and across the survey domain spanning the experiment. Primary changes were
310 development of near surface winds, and a slight increase in the PBL. AMOG Surveyor and AJAX
311 collected pre-survey intercomparison vertical profiles ~30 km north of the Kern Fields between the small
312 town of Delano on the SJV floor (100 m) up to a meadow (2058 m) above Shirley Meadows on a ridge of

313 the Greenhorn Mountains in the Sierra Nevada Mountain Range (Fig. 3). This profile spans a wide range
314 of topography, from grasslands on rolling hills, to tall pine trees near Alta Sierra, see Supp. Fig. S5 for
315 surface images along the profile. AMOG Surveyor also conducted a post-survey, downwind vertical
316 atmospheric profile to 1800 masl. Approximately 15 minutes of data were collected in an open (200–300
317 m) field above Shirley Meadows that was fairly exposed with only thin stands of pine trees on terrain
318 falling steeply off to both sides. The wind direction and speeds for the field were consistent with winds at
319 Alta Sierra, several hundred meters below, where AMOG was surrounded by tall trees. The field was
320 above the top of the AJAX profile.

321
322 FIGURE 3
323
324 AMOG Surveyor’s vertical ascent was collected before the AJAX profile to enable concurrent
325 AMOG/AJAX data collection for the Kern Fields. The AMOG Surveyor ascent/descent was from 18:48
326 to 21:09 (20:08 UTZ at crest), while AJAX flew a descent pattern from 20:58 to 21:04 UTC. AMOG
327 Surveyor’s descent was shortened to ~1000 m altitude (Glenville, CA) to allow AMOG to reach the Kern
328 Fields nearly concurrent with AJAX and GOSAT.

329
330 AMOG and AJAX profile data overlapped between 500 and 2000 m. There was very good agreement
331 between the two platforms for CO₂ and CH₄ for altitudes between 1.55 and 2 km (Fig. 4a and 4b), 99.9%
332 and 99.7%. AMOG and AJAX CH₄ concentrations decreased notably from the well-mixed PBL to the
333 near surface layer, from ~2.07 ppm (500-750 m) to ~1.93 ppm (250-300 m). AJAX also showed a
334 decrease in CO₂ from 403 ppm to below 400 ppm. The CO₂ decrease was consistent with a shift to
335 agricultural air where CO₂ vegetative uptake reduces CO₂ concentrations. The PBL grew from 600 to 900
336 m between AMOG’s ascent and descent and then to 1500 m by the time of AJAX’s descent based on the
337 CH₄, CO₂, and O₃ data.

338
339 FIGURE 4
340
341 The PBL was identified at ~1580-1600 m based on both surface and airborne relative humidity (*RH*) and
342 temperature (*T*) vertical profiles. Winds were not useful for deriving the location of the PBL. Diurnal
343 heating is apparent between the two AMOG Surveyor *T* profiles, but does not change the lapse rate.
344 Because AJAX flies above the surface where AMOG collects data, AJAX temperatures are lower. In the
345 lower atmosphere, the lapse rate was 6.9°C km⁻¹ for AJAX between 500-900 m, while the AMOG lapse
346 rate from 200-900 m was a similar 5.6°C km⁻¹. Between 950 and the top of the PBL, AMOG lapse rates

347 were much shallower, $2.5\text{ }^{\circ}\text{C km}^{-1}$, with a jump in temperature at 900 m. Above the PBL, the AMOG
348 measured lapse rate was $3.5^{\circ}\text{C km}^{-1}$, close to the wet adiabatic lapse rate (Fig. 4d).

349
350 Above the PBL, O_3 concentrations between AMOG and AJAX were ~ 20 ppb different although the
351 AMOG and AJAX profile slope ($d\text{O}_3/dz$) were the same. If the trend in AJAX $\text{O}_3(z)$ from 1600 to 1850 m
352 is extended to $z = 2058$ m (Fig. 3C, green arrow), there is agreement with AMOG Shirley Meadows (open
353 field) O_3 concentrations. This similar slope but different absolute value could indicate O_3 loss as it
354 diffused down through the pine canopy to the surface (and AMOG). Tall pine trees (30+ m) dominate
355 above ~ 1700 , except for Shirley Meadows where, as noted, there was good agreement. For $900 < z <$
356 1400 m, AJAX - AMOG agreement was better for the descent, which was closer in time to AJAX than
357 the ascent. This shift likely was associated with formation of the daytime PBL.

358
359 In this upwind profile, AJAX observed elevated O_3 that was well mixed down to 500 m, while earlier
360 AMOG showed well-mixed O_3 down to only 1100 m. There also was a small (~ 10 ppb) O_3 enhancement
361 at the top of the PBL in both the airborne and surface profiles. The highest O_3 concentrations were
362 observed by AMOG in Shirley Meadows, where visibility was low due to smoke aerosols from the Rough
363 Fire (NASA, 2015). Air above the PBL was more humid than elsewhere in the profile, except for the
364 lowest 50 m above the valley floor, which was enriched in CH_4 , CO_2 , and RH , possibly from nocturnal
365 accumulation and agriculture including irrigation RH inputs. There were thin layers in the atmosphere that
366 suggest remnant structures from the prior day. For example, at ~ 550 m the air changed character, with a
367 jump in CO_2 by ~ 10 ppm, and of O_3 by ~ 10 ppb, and a decrease in the CH_4 altitude gradient ($d\text{CH}_4/dz$).

368
369 Air was more polluted at greater altitude above the PBL in the upwind (Delano – Alta Sierra) profile for
370 O_3 for both platforms with air 10-20 ppb greater than in the PBL. Additionally, AJAX CH_4 and CO_2 were
371 significantly higher above the PBL. The AMOG CH_4 and CO_2 data are less clear, presumably because
372 AMOG data were prior to the disappearance of the nocturnal, stably stratified PBL. This was consistent
373 with visual observations of haze by AMOG from Shirley Meadows as well as by the AJAX pilot.
374 Additionally, air above the PBL was more humid.

375
376 FIGURE 5

377
378 A downwind ascent profile in the SJV was collected from Edison, CA to the high flanks of Breckenridge
379 Mountain, followed by a descent behind the Breckenridge Mountain to Caliente, CA through the tiny
380 town of Bodfish (Fig. 3b). This descent was separated from the SJV by a ridge and includes dryer, clean

381 air that is representative of air from around Lake Isabella, a fairly isolated mountain valley. The
382 downwind profile was collected quasi-Lagrangian in that the time separating the two profiles (about four
383 hours) is comparable to the transport time (75 km at a mean wind speed of 4 m s^{-1} , implies 5 hours for
384 transport). Thus, the downwind profile was for close to the same air. Over these hours, there was some
385 additional PBL growth, $\sim 100 \text{ m}$ growth to $\sim 1675 \text{ m}$, with highly uniform CH_4 between 1000 m and the
386 top of the PBL (**Fig. 5a**). Thus, the PBL remained fairly stable over the course of the study. Air in both
387 the upper PBL and above was cleaner with lower humidity and CH_4 concentrations. Unfortunately, the O_3
388 analyzer overheated during the ascent and resumed collecting data on the descent at $\sim 1500 \text{ m}$.

389

390 **FIGURE 6**

391

392 Direct comparison between AMOG and AJAX winds is inappropriate because AMOG winds are affected
393 strongly by obstacles including hills, trees, and buildings. However, in many instances, terrain is open or
394 gently rolling hills and there tend to be regions of stronger winds that we propose are representative of
395 free atmosphere winds. AMOG data were altitude binned and the strongest winds in each bin were
396 compared with AJAX (Fig. 6). Agreement is generally good (within 15-20%) between the upper 5% of
397 AMOG cross-slope (west) winds in each altitude-averaged band (Fig. 6a). For the upslope wind (north)
398 agreement is better (within 5-10%) for a larger range of altitudes (Fig. 6b). This allows fusions of the
399 upper 5% of AMOG winds with AJAX winds. Over the full altitude range, the median differences were
400 38% and 27% for the north and east wind components, see Supp. Fig. S7 for the altitude variation in the
401 agreement.

402 **3.2. Kern Fields and Bakersfield Greenhouse Gas Emissions**

403 **3.2.1 Methane**

404 On 19 Aug. 2015, winds over the Kern Fields were prevailing (northwesterly) and fairly strong ($\sim 3 \text{ m s}^{-1}$)
405 on the ground and somewhat stronger aloft (Fig. 7). Potential plumes from the only nearby upwind dairy
406 (Fig. 7a, white arrow) were directed by winds to pass to the west of the oil fields, agricultural fields in this
407 part of the SJZ are dry. As a result, surface topography like the Kern River Bluffs imposed only small
408 wind modification at the surface and at altitude. Southeast of Bakersfield, winds veered to westerlies
409 towards passes in the Sierra Nevada Mountains that connect to the Mojave Desert. The downwind survey
410 included two plume transits on agricultural roads with negligible to no traffic. These transits clearly show
411 the plume's eastward drift, passing to the north of the small town of Arvin, CA.

412

413 The background CH₄ plane $C_B(x,z)$ was extracted from the CH₄ data outside the plume – $C_{BL}(z)$ and
414 $C_{BR}(z)$, see Eqn. (2) – immediately downwind of the Kern Fields (transect $\gamma-\gamma'$). C_B showed a slight
415 increase towards the east of ~20 ppb (Supp. Fig. S6a). The normal wind (U_n) was fairly uniform across
416 the data plane, including downwind of the canyon (Fig. 8e). Thus, the CH₄ flux ($Q_{CH_4}(x, z)$) shows similar
417 spatial patterns to CH₄'(x, z). Emissions from the Kern Fields' were dominated by a large, focused CH₄
418 plume (or group of plumes) in the core of a much broader, dispersed, and poorly defined plume. This
419 structure is evident in both surface AMOG data and in the lowest AJAX altitude for plane $\gamma-\gamma'$ with both
420 showing the strongest peak at $x = 4.5$ km (Fig. 8b, dashed lines). Total estimated emissions (E) were
421 $63.5 \pm 50\%$ Mol s⁻¹ (equivalent to 32 Gg yr⁻¹). Uncertainty is from the Monte Carlo simulations, described
422 in section 2.5.

423

424 FIGURE 7

425

426 FIGURE 8

427

428 Within the plume, concentrations are elevated at 1200 m altitude relative to 500 m and the surface,
429 indicating buoyant rise. Additional evidence for buoyant rise is provided by two small plumes at $x \sim 1.7$
430 and 5.7 km were centered at the top of the PBL but were not also observed in surface and mid altitude
431 data. The upper AJAX flight line was several hundred meters below the top of the PBL (at ~1580 m, Fig.
432 4), which constrains the main plume and was centered vertically in the PBL. Concentrations above the
433 PBL were determined from AJAX descent and ascent data (Fig. 4), in agreement with AMOG data above
434 the PBL. These observations show that the plume was not well mixed across the PBL. Another important
435 feature is the upper altitude clean air intrusion at $x \sim 6.5$ km lies downwind of Round Mountain Canyon to
436 the east of the Kern River oil field (Fig. 8b, Fig. 7a for location). This intrusion does not penetrate down
437 to 500 m and represents a downslope airflow of cleaner upper level air.

438

439 For comparison, a recent bottom-up estimate of CH₄ emissions based on production data for the Kern
440 Fields estimated 10-40 Gg CH₄ yr⁻¹ (68% Confidence Level), by combining oil and gas production data
441 with US-EPA emissions factors for associated wells (Jeong et al., 2014). Other CH₄ sources are unlikely
442 to confuse this interpretation as petroleum system emissions are ~20 times larger than estimated nearby
443 livestock and landfill CH₄ emissions of ~2.3 and 1.4 Gg yr⁻¹, respectively (Calgem, 2014).

444 3.2.2. Carbon Dioxide

445 Background CO₂ for data curtain $\gamma-\gamma'$ (Supp. Fig. S6b) was highly uniform. Given the strong crosswinds
446 and care taken to avoid trailing other vehicles on the low-trafficked China Loop Road, these data passed
447 quality review – CO₂ exhaust contamination manifests as a dramatic increase in the standard deviation
448 whenever AMOG intersects a vehicle exhaust's turbulent plume. There was a shallow CO₂ layer
449 constrained to the lower 100 to 200 m with ~10 ppm enhancement (Fig. 9a), also observed in the CO₂
450 vertical profile (Fig. 4b), a layer that was characterized by elevated relative humidity. Further evidence
451 that these broad spatial CO₂ emissions are real is from the spatial similarity to CO₂ enhancements in the
452 lowest AJAX flight data (Fig. 9c). For example, the surface CO₂ plume was strongest at $x \sim 4.5$ km in
453 AMOG and AJAX data. The broad spatial extent of these emissions, similar to the broad CH₄ emissions
454 suggests a relationship to field-scale (engineering or geological) processes. Overall CO₂ emissions were
455 $1730 \pm 50\%$ Mol s⁻¹ (equivalent to 2.4 ± 1.2 Tg yr⁻¹).

456

457 FIGURE 9

458

459 There was a strong CO₂ anomaly in a focused plume at $x = 5$ km and $z = 1$ km. This plume likely relates
460 to the two cogeneration power plants located in the Kern River oil field. Further support for this
461 interpretation is its co-location with a similarly focused CH₄ plume at the same location. This power
462 plant-related feature is a persistent feature that has been observed in other surveys (Leifer – unpublished
463 data). The upper clean air intrusion in the CH₄ data curtain also is apparent in the CO₂ data (Fig. 9b), in
464 front of Round Mountain Canyon (Fig. 7).

465

466 Based on a reservoir CO₂:CH₄ gas ratio of 92.2%:1.7% (Lillis et al., 2008) and 32 Gg yr⁻¹ CH₄ emissions,
467 the Kern Fields' CO₂ emissions were predicted to be 1.8 Tg yr⁻¹, which is fairly consistent with the
468 directly derived emissions of 2.4 Tg yr⁻¹. Both these values are somewhat lower than the inventory for the
469 cogeneration plants in Kern River oil field, 3.1 Tg yr⁻¹ (CARB, 2016). The disagreement with inventory
470 likely arises from the co-generation plant only being active some of the time, confirmed by data from the
471 GOSAT-COMEX campaign.

472

473 4. Discussion

474 4.1. Experimental design and real-time visualization

475 Ideally, GCE airborne and surface data are collected first upwind and then downwind. However, AJAX
476 airborne data are not collected in a Lagrangian sense as would be necessary for slower, less maneuverable
477 airborne platform thanks to its extreme speed and maneuverability. This allows collection of near
478 snapshot (~30 minutes) data. Slower, AMOG surface data were collected in a quasi-Lagrangian sense,
479 reducing the likelihood of confounding interference in the study area from non-FFI SJV inputs due to
480 wind shifts after the pre-survey (for non-nominal winds the collection is aborted). Given the AJAX-
481 AMOG speed difference, concurrent surface and airborne data could not be collected both upwind and
482 downwind, and thus, concurrency was prioritized for downwind. For flight efficiency and to provide
483 downwind concurrency with AMOG, AJAX flew a triangle that allowed AJAX to complete transects at
484 three altitudes in close to AMOG's upwind-downwind survey time.

485
486 After the Kern Fields survey, AJAX returned to base, while AMOG collected additional surface data,
487 exploring the fate of emissions from the Kern Fields. The word, "exploring" is significant, as real-time
488 visualization of winds, CH₄, and O₃ guided the downwind surveying. Data were collected to test the
489 hypothesis that there was a relationship between wind strength and the specific outflow path from the SJV
490 to Mojave Desert - specifically, that more northerly passes, which require greater wind veering from
491 prevailing are preferred at lower winds speeds. The AMOG survey first confirmed that outflow was not
492 up the Kern River Valley, and then collected a downwind vertical profile into the Sierra Nevada
493 Mountains to search for outflow through a pass near Breckenridge Mountain. After confirming its
494 absence, AMOG then investigated in the Tehachapi Pass, where the outflow was identified. Thus, on 19
495 Aug. 2015, when winds were strong, the outflow was by the most direct pathway - the Tehachapi Pass.

496 4.2. Experimental design and uncertainty reduction

497 The experimental design reduced uncertainty by characterizing the PBL through surface and airborne data
498 fusion so that a well-mixed PBL is not required. Note, for a well-mixed PBL, surface-airborne data fusion
499 does not reduce uncertainty. The benefit arises for a not well-mixed PBL where a significant fraction of
500 the plume mass lies below the lowest altitude the airplane can fly. In such case, surface data inclusion
501 adds information to the PBL characterization. For example, flights can face airspace restrictions in cities,
502 airport approaches, military airspace, and/or for safety.

503

504 Aerial survey altitudes were designed to span from near the top of the PBL to as low as permissible and
505 include an intermediate level (0.5, 1, 1.2 km). Thus, surface data added information on the lowest third of
506 the 1.6-km thick PBL. This lower portion of the PBL is more important on days when the PBL is
507 shallower.

508
509 Observations showed that the well-mixed PBL assumption was poor as far as 10-20 km downwind. One
510 solution is to collect data even further downwind, where the PBL should be better mixed (White et al.,
511 1976); however, secondary (potentially uncharacterized) sources downwind of the study area and upwind
512 of the downwind data plane add confounding anomalies. Also, wind flow complexity can lead to transport
513 orthogonal to the overall downwind direction, leading to flux leakage out of the plume. The likelihood of
514 plume loss increases over greater distances. And finally, as the PBL evolves with time, it imposes an
515 evolving structure on the wind and concentration vertical profiles, which also challenge the well-mixed
516 PBL assumption – particularly if transport to the downwind plane requires hours.

517
518 The *in situ* analyzers record concentration and winds with very high accuracy; however, only at a single
519 location and time. Thus, *in situ* uncertainty arises mostly from inadequate characterization of temporal
520 variability and spatial heterogeneity in winds and emissions over the survey time period. The best strategy
521 is to minimize study time; however, there is a necessary tradeoff between spatial resolution and study
522 time. AJAX collects data quickly, allowing survey completion within far less than typical atmospheric
523 change timescales. Similarly, the surface survey route was designed to minimize collection time,
524 primarily on rural/agricultural roads carefully selected to avoid traffic congestion and traffic lights. The
525 surface survey requires ~90 minutes to complete and is conducted quasi-Lagrangian.

526
527 GCE treats uncertainty explicitly, allowing improvements in the data collection strategy to reduce
528 uncertainty. For example, the east-west downwind transect was lengthened from earlier data collects to
529 characterize background concentrations better. GCE also does not require an *a priori* emission
530 distribution and thus incorporates explicitly emissions from super-emitters, normal emitters, and
531 distributed sources, improving robustness of the findings. In contrast, inversion models require a
532 reasonable spatial *a priori* emission distribution and the ability to model transport across the study
533 domain. However, complex wind flows from fine-scale topographic structures, as observed for the Kern
534 Fields, challenge transport modeling.

535 **4.3. Profile intercomparison**

536 This study leveraged terrain to provide profile information with a surface mobile platform, which was
537 compared with airborne data. In this study, the two were combined to provide more complete coverage of
538 the atmosphere than a single platform could, at a fraction of the cost (not to mention logistical
539 complexity) of having two airborne platforms. Whereas the approach worked well in the San Joaquin
540 Valley, further research is needed to confirm its utility in other settings.

541
542 Above the PBL, there was excellent agreement between surface and airborne concentration profile data,
543 while concentration profiles within the PBL show significant differences between the two profiles, likely
544 related to air mass shifts and diurnal heating during the time between the profiles (Fig. 4). Winds above
545 the PBL were in poor agreement, with the north component in the opposite direction (Fig. 6). Underlying
546 this discrepancy was a mountain peak, which clearly caused large-scale alterations in the wind flow field.

547
548 Within the PBL, agreement between unfiltered surface AMOG winds and AJAX winds was poor,
549 unsurprising because surface winds are strongly affected by obstacles. However, by filtering AMOG
550 winds (collected 3-m above the surface) for the strongest 5%, agreement was within 15-20% for the
551 along-slope – i.e., north – winds, and better for upslope winds (west). Specific exceptions were when
552 AMOG was in a dense grove of pines, and when AJAX flew behind into the lee of a mountain peak.
553 Surface winds are modulated by a wide range of surface factors including trees, steep hills and hillocks,
554 blocking by a steep slope, rolling hills, and structures (Supp. Fig S5). However, a combination of gusts
555 (among thin wooded terrain on steep slopes) and the limited spatial extent of most obstacles underlies the
556 agreement between the filtered AMOG and AJAX wind profiles. Agreement is better for the upper
557 portions of the PBL (within 10-20%) where Sierra Nevada Mountain slopes are steeper. In contrast, the
558 slope lower in the PBL is gentle, and surface boundary layer effects are more pronounced, biasing wind
559 speeds slower.

560
561 The wind orientation to the slope affects the comparison because topography imposes wind-field structure
562 at large and small scales. Where winds advect air upslope, transport incorporates a non-negligible vertical
563 component that is missed by the 2D sonic anemometer used in the study reported here. Currently, AMOG
564 measures 3D winds, as does AJAX.

565
566 Some of the discrepancy between AMOG and AJAX wind profiles could have arisen from temporal
567 changes between the two profiles; however, this is unlikely for two reasons. First, the top of the PBL was

568 identified four times over the course of the study and remained stable within 100 m across the domain.
569 And second, surface wind observations remained relatively constant after the mid-morning shift to
570 daytime conditions (breakup of nocturnal stratification). However, the poor agreement between AJAX
571 and AMOG vertical concentration profiles within the PBL suggests significant air mass shifts –
572 highlighting the need for better concurrence.

573 **4.4. GHG FFI emissions**

574 Emissions for the Kern Fields were estimated at 32 ± 16 Gg $\text{CH}_4 \text{ yr}^{-1}$ with CH_4 emissions ~20% above
575 EPA inventories, and 2.4 ± 1.2 Tg $\text{CO}_2 \text{ yr}^{-1}$. The broad CO_2 plume suggests emissions from the geologic
576 reservoir – likely along the same pathways associated with CH_4 leakage – in addition to the focused and
577 not continuous emissions from the co-generation power plants. On China Loop Road (where the CO_2
578 surface plume was transected), strong crosswinds and light traffic would have prevented significant
579 vehicular CO_2 contamination. Additionally there are no upwind (non-oil field) roads, only the foothills of
580 the Sierra Nevada Mountains.

581
582 For comparison, a recent bottom-up estimate of CH_4 emissions from the Kern Fields estimated 25 ± 15 Gg
583 $\text{CH}_4 \text{ yr}^{-1}$ by combining oil and gas production data with emissions factors for associated wells used by
584 US-EPA (Jeong et al., 2014), i.e., 19 Aug. 2015 CH_4 emissions were a third above inventories. The
585 derived flux lies within the inventory uncertainty, but is higher, consistent with a recent metastudy of
586 field studies of FFI production emissions, which showed significant underestimation in the EPA budget
587 (Brandt et al., 2014; Miller et al., 2013). A number of factors likely play a role including the age of the
588 Kern River oil field (over a century), production factors (steam injection), shallowness of the reservoir
589 (<300 m), location in a tectonically active area, which creates alternate migration pathways from the
590 reservoir (Leifer et al., 2013), and the recent expansion of the number of wells in the Kern Front oil field
591 (from GoogleEarth timeline imagery). Many of these factors are common to other production fields in
592 California, the US, and globally. Given the importance of FFI to the overall budget, even small
593 underestimation could be highly significant. Thus, this uncertainty highlights the need for improved
594 measurement tools to reduce the significant uncertainty in the CH_4 budget and for satellite measurement
595 validation, particularly for complex terrain and in the source's near field.

596 **5. Conclusion**

597 This study showed how to combine airborne and surface *in situ* data to improve emissions derivation, and
598 demonstrated the novel use of topography to characterize vertical atmospheric structure with a surface

599 mobile platform. Given that mountains cover a significant fraction of the earth's land surface, further
 600 research should be undertaken to confirm that this approach applies in other settings. Data showed the
 601 PBL was not well mixed, even 10-20 km downwind, highlighting the importance of the direct flux
 602 quantification approach. Direct quantification does not require accurate modeling of winds across
 603 complex terrain, but does require interpolation and data modeling to identify the background.

604

605 **Table of Nomenclature**

606		Units	Description
607	AJAX	(-)	Alpha Jet Atmospheric eXperiment
608	AMOG	(-)	AutoMOBILE trace Gas
609	Bbl	(-)	Barrel (of oil) 1 bbl = 6.38 m ³
610	COMEX	(-)	CO ₂ and METHane eXperiment
611	EOR	(-)	Enhanced oil recovery (techniques)
612	EPA	(-)	Environmental Protection Agency
613	GCE	(-)	GOSAT COMEX Experiment
614	GHG	(-)	Greenhouse Gases
615	GOSAT	(-)	Greenhouse gases Observing SATellite
616	GHG	(-)	Greenhouse gas
617	PBL	(-)	Planetary Boundary Layer
618	SJV	(-)	San Joaquin Valley
619	Tg		Terragram (10 ¹² g)
620	UTZ	(-)	Universal time
621	$C'(x,z)$	(ppm)	concentration anomaly (above C_B)
622	$C(x,z)$	(ppm)	concentration
623	$C_B(x,z)$	(ppm)	background concentration – outside plume
624	$C_{BL}(z)$	(ppm)	background concentration profile – left side of profile
625	$C_{BR}(z)$	(ppm)	background concentration profile – right side of profile
626	E	(mol s ⁻¹)	Emission source strength
627	$k(z)$	(mol ppm ⁻¹)	Conversion factor from the ideal gas law
628	N'	(mol cm ⁻³)	molar mass anomaly
629	$Q(x,z)$	(mol m ⁻² s ⁻¹)	Flux through the data plane
630	R^2	(-)	Correlation coefficient
631	RH	(%)	Relative humidity
632	T	(°C)	Temperature

633	$U_n(x,z)$	(m s ⁻¹)	Winds normal to the data plane, a function of (x, z)
634	U_{north}	(m s ⁻¹)	North wind component
635	U_{west}	(m s ⁻¹)	West wind component
636	x	(m)	lateral distance – approximately cross-wind
637	x_L	(m)	left half of the transect ($x < x_{max}/2$)
638	x_{max}	(m)	length of a transect
639	x_R	(m)	right half of the transect ($x > x_{max}/2$)
640	y	(m)	lateral distance – approximately co-wind
641	z	(m)	altitude
642	$\Phi_L(C)$	(-)	concentration probability distribution for left side of transect
643	$\Phi_R(C)$	(-)	concentration probability distribution for right side of transect
644	$\Phi_P(C)$	(-)	concentration probability distribution for the plume
645	$\Phi_B(C)$	(-)	concentration probability distribution for the background
646	α, α'	(-)	designation for Delano – Alta Sierra surface transect
647	$\varepsilon, \varepsilon'$	(-)	designation for Edison– Breckenridge Mtn. surface transect
648	τ, τ'	(-)	designation for Breckenridge – Caliente surface transect
649	β, β', β_1'	(-)	designation for Wasco – Granite surface transect
650	γ, γ'	(-)	designation for Oildale – Oil City surface and airborne transects
651	δ, δ'	(-)	designation for Ming Park – Arvin surface and airborne transects

652

653 **Data Availability.** Data will be provided as per the data policy.

654

655 **Author Contribution.** I. Leifer prepared the manuscript with input from all co-authors. C. Melton
656 prepared figures and conducted data analysis. M. Fischer helped prepare the emissions budgets. J. Frash
657 helped with AMOG data collection. L. Iraci, J. Marrero, J-M. Ryoo, T. Tanaka, and E. Yates are part of
658 the AJAX team and worked to collect and analyze AJAX data.

659

660 There are no competing interests

661

662 **Acknowledgements:** We thank the NASA Earth Science Division, Research and Analysis Program, grant
663 NNX13AM21G. MLF was supported by a grant from the California Energy Commission’s Natural
664 Gas Research Program to the Lawrence Berkeley National Laboratory under contract DE-AC02-

665 36605CH11231. AJAX data were collected under the AJAX project, which acknowledges the partnership
666 of H211, LLC and support from the Ames Research Center Director's funds.
667

668 6. References

- 669 Allen, G.: Biogeochemistry: Rebalancing the global methane budget, *Nature*, 538, 46-48, 2016.
670 American Lung Association: State of the Air, 2016, American Lung Association, Chicago, IL,
671 157 pp., 2016.
- 672 Bao, J. W., Michelson, S. A., Persson, P. O. G., Djalalova, I.V., and Wilczak, J. M.: Observed
673 and WRF-simulated low-level winds in a high-ozone episode during the Central California
674 Ozone Study, *Journal of Applied Meteorology and Climatology*, 47, 2372-2394, 2008.
- 675 Boucouvala, D. and Bornstein, R.: Analysis of transport patterns during an SCOS97-NARSTO
676 episode, *Atmospheric Environment*, 37, Supplement 2, 73-94, 2003.
- 677 Brandt, A. R., Heath, G. A., Kort, E. A., O'Sullivan, F., Pétron, G., Jordaan, S. M., Tans, P.,
678 Wilcox, J., Gopstein, A. M., Arent, D., Wofsy, S., Brown, N. J., Bradley, R., Stucky, G. D.,
679 Eardley, D., and Harriss, R.: Methane leaks from North American natural gas systems,
680 *Science*, 343, 733-735, 2014.
- 681 Calgem: California Greenhouse Gas Emissions Measurement (CALGEM) Project. DOE, 2014.
- 682 CARB: Facility GHG Emissions Visualization and Analysis Tool: 2008-2014. California
683 Environmental Protection Agency, Air Resources Board, 2016.
- 684 Chen, H., Winderlich, J., Gerbig, C., Hofer, A., Rella, C. W., Crosson, E. R., Van Pelt, A. D.,
685 Steinbach, J., Kolle, O., Beck, V., Daube, B. C., Gottlieb, E. W., Chow, V. Y., Santoni, G.
686 W., and Wofsy, S. C.: High-accuracy continuous airborne measurements of greenhouse gases
687 (CO₂ and CH₄) using the cavity ring-down spectroscopy (CRDS) technique, *Atmos. Meas.*
688 *Tech.*, 3, 375-386, 2010.
- 689 Dlugokencky, E. J., Crotwell, A., Masarie, K., White, J., Lang, P., and Crotwell, M.: NOAA
690 Measurements of Long-lived Greenhouse Gases, Asia-Pacific GAW Greenhouse Gases, 6, 6-
691 9, 2013.
- 692 Dlugokencky, E. J., Nisbet, E. G., Fisher, R., and Lowry, D.: Global atmospheric methane:
693 Budget, changes and dangers, *Philosophical Transactions of the Royal Society A:*
694 *Mathematical, Physical and Engineering Sciences*, 369, 2058-2072, 2011.
- 695 EPA: 2013 Inventory of US greenhouse gas: Emissions and sinks: 1990-2011, Environmental
696 Protection Agency, Washington DC, 457 pp., 2013.
- 697 EPA: 2017 Inventory of US greenhouse gas: Emissions and sinks: 1990-2015, Environmental
698 Protection Agency, Washington DC430-P-17-001, 633 pp., 2017.
- 699 European Commission: Emission Database for Global Atmospheric Research (EDGAR). Joint
700 Research Centre (JRC)/Netherlands Environmental Assessment Agency (PBL), 2010.
- 701 Farrell, P., Leifer, I., and Culling, D.: Transcontinental methane measurements: Part 1. A mobile
702 surface platform for source investigations, *Atmospheric Environment*, 74, 422-431, 2013.
- 703 Fernandez-Cortes, A., Cuezva, S., Alvarez-Gallego, M., Garcia-Anton, E., Pla, C., Benavente,
704 D., Jurado, V., Saiz-Jimenez, C., and Sanchez-Moral, S.: Subterranean atmospheres may act
705 as daily methane sinks, *Nature Communication*, 6, 2015.

706 Gentner, D. R., Ford, T. B., Guha, A., Boulanger, K., Brioude, J., Angevine, W. M., de Gouw, J.
707 A., Warneke, C., Gilman, J. B., Ryerson, T. B., Peischl, J., Meinardi, S., Blake, D. R., Atlas,
708 E., Lonneman, W. A., Kleindienst, T. E., Beaver, M. R., Clair, J. M. S., Wennberg, P. O.,
709 VandenBoer, T. C., Markovic, M. Z., Murphy, J. G., Harley, R. A., and Goldstein, A. H.:
710 Emissions of organic carbon and methane from petroleum and dairy operations in
711 California's San Joaquin Valley, *Atmospheric Chemistry and Physics*, 14, 4955-4978, 2014.

712 Ghosh, A., Patra, P. K., Ishijima, K., Umezawa, T., Ito, A., Etheridge, D. M., Sugawara, S.,
713 Kawamura, K., Miller, J. B., Dlugokencky, E. J., Krummel, P. B., Fraser, P. J., Steele, L. P.,
714 Langenfelds, R. L., Trudinger, C. M., White, J. W. C., Vaughn, B., Saeki, T., Aoki, S., and
715 Nakazawa, T.: Variations in global methane sources and sinks during 1910–2010,
716 *Atmospheric Chemistry and Physics*, 15, 2595-2612, 2015.

717 Hamill, P., Iraci, L. T., Yates, E. L., Gore, W., Bui, T. P., Tanaka, T., and Loewenstein, M.: A
718 new instrumented airborne platform for atmospheric research, *Bulletin of the American*
719 *Meteorological Society*, 97, 2015.

720 IPCC: Climate Change 2007: Synthesis Report. Contribution of Working Groups I, II, and III to
721 the Fourth Assessment Report of the Intergovernmental Panel on Climate Change, IPCC,
722 Geneva, Switzerland, 104 pp., 2007.

723 IPCC: Working Group 1 Contribution to the IPCC Fifth Assessment Report Climate Change
724 2013-The Physical Science Basis, International Panel on Climate Change, IPCC Secretariat,
725 Geneva, Switzerland, 2216 pp., 2013.

726 Jeong, S., Hsu, Y.-K., Andrews, A. E., Bianco, L., Vaca, P., Wilczak, J. M., and Fischer, M.:
727 Multi-tower measurement network estimate of California's methane emissions, *Journal of*
728 *Geophysical Research - Atmospheres*, 118, 2013JD019820, 2013.

729 Jeong, S., Zhao, C., Andrews, A. E., Bianco, L., Wilczak, J. M., and Fischer, M. L.: Seasonal
730 variation of CH₄ emissions from central California, *Journal of Geophysical Research*, 117,
731 2012.

732 Jeong, S. S., Millstein, D., and Fischer, M. L.: Spatially explicit methane emissions from
733 petroleum production and the natural gas system in California, *Environmental Science &*
734 *Technology*, 48, 5982-5990, 2014.

735 John, J. G., Fiore, A. M., Naik, V., Horowitz, L. W., and Dunne, J. P.: Climate versus emission
736 drivers of methane lifetime against loss by tropospheric OH from 1860–2100, *Atmospheric*
737 *Chemistry and Physics*, 12, 12021-12036, 2012.

738 Karion, A., Sweeney, C., Pétron, G., Frost, G., Michael Hardesty, R., Kofler, J., Miller, B. R.,
739 Newberger, T., Wolter, S., Banta, R., Brewer, A., Dlugokencky, E., Lang, P., Montzka, S. A.,
740 Schnell, R., Tans, P., Trainer, M., Zamora, R., and Conley, S.: Methane emissions estimate
741 from airborne measurements over a western United States natural gas field, *Geophysical*
742 *Research Letters*, 40, 4393-4397, 2013.

743 Karlsdóttir, S. and Isaksen, I. S. A.: Changing methane lifetime: Possible cause for reduced
744 growth, *Geophysical Research Letters*, 27, 93-96, 2000.

745 Khalil, M. A. K. and Rasmussen, R. A.: The changing composition of the Earth's atmosphere.
746 In: *Composition, chemistry, and climate of the atmosphere*, Singh, H. B. (Ed.), Van Nostrand
747 Reinhold, New York, 1995.

748 Kirschke, S., Bousquet, P., Ciais, P., Saunois, M., Canadell, J. G., Dlugokencky, E. J.,
749 Bergamaschi, P., Bergmann, D., Blake, D. R., and Bruhwiler, L.: Three decades of global
750 methane sources and sinks, *Nature Geoscience*, 6, 813-823, 2013.

751 Krautwurst, S., Gerilowski, K., Krings, T., Borchard, J., Bovensmann, H., Leifer, I., Fladland,
752 M. M., Koyler, R., Iraci, L. T., Luna, B., Thompson, D. R., Eastwood, M., Green, R.,
753 Jonsson, H. H., Vigil, S. A., and Tratt, D. M.: COMEX - Final Report: Scientific and
754 Technical Assistance for the Deployment of a flexible airborne spectrometer system during
755 CMAPEXP and COMEX, IUP-COMEX-FR, 148 pp., 2016.

756 Krings, T., Gerilowski, K., Buchwitz, M., Reuter, M., Tretner, A., Erzinger, J., Heinze, D.,
757 Pflüger, U., Burrows, J. P., and Bovensmann, H.: MAMAP – a new spectrometer system for
758 column-averaged methane and carbon dioxide observations from aircraft: Retrieval algorithm
759 and first inversions for point source emission rates, *Atmospheric Measurement Techniques*,
760 4, 1735-1758, 2011.

761 LaFranchi, B. W., Pétron, G., Miller, J. B., Lehman, S. J., Andrews, A. E., Dlugokencky, E. J.,
762 Hall, B., Miller, B. R., Montzka, S. A., Neff, W., Novelli, P. C., Sweeney, C., Turnbull, J. C.,
763 Wolfe, D. E., Tans, P. P., Gurney, K. R., and Guilderson, T. P.: Constraints on emissions of
764 carbon monoxide, methane, and a suite of hydrocarbons in the Colorado Front Range using
765 observations of $^{14}\text{CO}_2$, *Atmos. Chem. Phys.*, 13, 11101-11120, 2013.

766 Lamb, B. K., McManus, J., Shorter, J., Kolb, C., Mosher, B., Harriss, R., Allwine, E., Blaha, D.,
767 Howard, T., Guenther, A., Lott, R., Siverson, R., Westburg, H., and Zimmerman, P.:
768 Development of atmospheric tracer methods to measure methane emissions from natural gas
769 facilities and urban areas, *Environmental Science & Technology*, 29, 1468-1479, 1995.

770 Leen, J. B., Yu, X. Y., Gupta, M., Baer, D. S., Hubbe, J. M., Kluzek, C. D., Tomlinson, J. M.,
771 and Hubbell, M. R., 2nd: Fast in situ airborne measurement of ammonia using a mid-infrared
772 off-axis ICOS spectrometer, *Environmental Science & Technology*, 47, 10446-10453, 2013.

773 Leifer, I., Culling, D., Schneising, O., Farrell, P., Buchwitz, M., and Burrows, J.:
774 Transcontinental methane measurements: Part 2. Mobile surface investigation of fossil fuel
775 industrial fugitive emissions, *Atmospheric Environment*, 74, 432-441, 2013.

776 Leifer, I., Melton, C., Frash, J., Fischer, M. L., Cui, X., Murray, J. J., and Green, D. S.: Fusion of
777 mobile in situ and satellite remote sensing observations of chemical release emissions to
778 improve disaster response, *Frontiers in Science*, 4, 1-14, 2016.

779 Leifer, I., Melton, C., Manish, G., and Leen, B.: Mobile monitoring of methane leakage, *Gases*
780 *and Instrumentation*, July/August 2014, 20-24, 2014.

781 Lillis, P. G., Warden, A., Claypool, G. E., and Magoon, L. B.: Petroleum systems of the San
782 Joaquin Basin Province -- geochemical characteristics of gas types: Chapter 10. In:
783 Petroleum systems and geologic assessment of oil and gas in the San Joaquin Basin Province,
784 California, Scheirer, A. H. (Ed.), 1713-10, U. S. Geological Survey, Reston, VA, 2008.

785 McKain, K., Down, A., Raciti, S. M., Budney, J., Hutyra, L. R., Floerchinger, C., Herndon, S.
786 C., Nehrkorn, T., Zahniser, M. S., Jackson, R. B., Phillips, N., and Wofsy, S. C.: Methane
787 emissions from natural gas infrastructure and use in the urban region of Boston,
788 Massachusetts, *Proceedings of the National Academy of Sciences*, 2015. 2015.

789 Miller, S. M., Wofsy, S. C., Michalak, A. M., Kort, E. A., Andrews, A. E., Biraud, S. C.,
790 Dlugokencky, E. J., Eluszkiewicz, J., Fischer, M. L., Janssens-Maenhout, G., Miller, B. R.,
791 Miller, J. B., Montzka, S. A., Nehrkorn, T., and Sweeney, C.: Anthropogenic emissions of
792 methane in the United States, *Proceedings of the National Academy of Sciences*, 110, 20018-
793 20022, 2013.

794 NASA: <https://www.nasa.gov/image-feature/goddard/wildfires-in-california-august-17-2015>, last
795 access: 16 April 2017, 2015.

796 Nisbet, E. G., Dlugokencky, E. J., and Bousquet, P.: Methane on the rise—Again, *Science*, 343,
797 493-495, 2014.

798 Nisbet, E. G., Dlugokencky, E. J., Manning, M. R., Lowry, D., Fisher, R. E., France, J. L.,
799 Michel, S. E., Miller, J. B., White, J. W. C., Vaughn, B., Bousquet, P., Pyle, J. A., Warwick,
800 N. J., Cain, M., Brownlow, R., Zazzeri, G., Lanoisellé, M., Manning, A. C., Gloor, E.,
801 Worthy, D. E. J., Brunke, E. G., Labuschagne, C., Wolff, E. W., and Ganesan, A. L.: Rising
802 atmospheric methane: 2007–2014 growth and isotopic shift, *Global Biogeochemical Cycles*,
803 30, 1356-1370, 2016.

804 Peischl, J., Karion, A., Sweeney, C., Kort, E. A., Smith, M., L., Brandt, A. R., Yeskoo, T.,
805 Aikin, K. C., Conley, S. A., and Gvakharia, A.: Quantifying atmospheric methane emissions
806 from oil and natural gas production in the Bakken shale region of North Dakota, *Journal of*
807 *Geophysical Research: Atmospheres*, 212, 2016.

808 Peischl, J., Ryerson, T. B., Aikin, K. C., de Gouw, J. A., Gilman, J. B., Holloway, J. S., Lerner,
809 B. M., Nadkarni, R., Neuman, J. A., Nowak, J. B., Trainer, M., Warneke, C., and Parrish, D.
810 D.: Quantifying atmospheric methane emissions from the Haynesville, Fayetteville, and
811 northeastern Marcellus shale gas production regions, *Journal of Geophysical Research:*
812 *Atmospheres*, 120, 2119-2139, 2015.

813 Peischl, J., Ryerson, T. B., Brioude, J., Aikin, K. C., Andrews, A. E., Atlas, E., Blake, D., Daube,
814 B. C., de Gouw, J. A., Dlugokencky, E., Frost, G. J., Gentner, D. R., Gilman, J. B.,
815 Goldstein, A. H., Harley, R. A., Holloway, J. S., Kofler, J., Kuster, W. C., Lang, P. M.,
816 Novelli, P. C., Santoni, G. W., Trainer, M., Wofsy, S. C., and Parrish, D. D.: Quantifying
817 sources of methane using light alkanes in the Los Angeles basin, California, *Journal of*
818 *Geophysical Research: Atmospheres*, 118, n/a-n/a, 2013.

819 Pétron, G., Frost, G., Miller, B. R., Hirsch, A. I., Montzka, S. A., Karion, A., Trainer, M.,
820 Sweeney, C., Andrews, A. E., Miller, L., Kofler, J., Bar-Ilan, A., Dlugokencky, E. J., Patrick,
821 L., Moore, C. T. J., Ryerson, T. B., Siso, C., Kolodzey, W., Lang, P. M., Conway, T.,
822 Novelli, P., Masarie, K., Hall, B., Guenther, D., Kitzis, D., Miller, J., Welsh, D., Wolfe, D.,
823 Neff, W., and Tans, P.: Hydrocarbon emissions characterization in the Colorado Front
824 Range: A pilot study, *J. Geophys. Res.*, 117, D04304, 2012.

825 Rigby, M., Montzka, S. A., Prinn, R. G., White, J. W. C., Young, D., O'Doherty, S., Lunt, M. F.,
826 Ganesan, A. L., Manning, A. J., Simmonds, P. G., Salameh, P. K., Harth, C. M., Mühle, J.,
827 Weiss, R. F., Fraser, P. J., Steele, L. P., Krummel, P. B., McCulloch, A., and Park, S.: Role
828 of atmospheric oxidation in recent methane growth, *Proceedings of the National Academy of*
829 *Sciences*, 114, 5373-5377, 2017.

830 Rigby, M., Prinn, R. G., Fraser, P. J., Simmonds, P. G., Langenfelds, R. L., Huang, J., Cunnold,
831 D. M., Steele, L. P., Krummel, P. B., Weiss, R. F., O'Doherty, S., Salameh, P. K., Wang, H.
832 J., Harth, C. M., Mühle, J., and Porter, L. W.: Renewed growth of atmospheric methane,
833 *Geophys. Res. Lett.*, 35, L22805, 2008.

834 Saunio, M., Bousquet, P., Poulter, B., Peregón, A., Ciais, P., Canadell, J. G., Dlugokencky, E.
835 J., Etiope, G., Bastviken, D., Houweling, S., Janssens-Maenhout, G., Tubiello, F. N.,
836 Castaldi, S., Jackson, R. B., Alexe, M., Arora, V. K., Beerling, D. J., Bergamaschi, P., Blake,
837 D. R., Brailsford, G., Brovkin, V., Bruhwiler, L., Crevoisier, C., Crill, P., Curry, C.,
838 Frankenberg, C., Gedney, N., Höglund-Isaksson, L., Ishizawa, M., Ito, A., Joos, F., Kim, H.
839 S., Kleinen, T., Krummel, P., Lamarque, J. F., Langenfelds, R., Locatelli, R., Machida, T.,
840 Maksyutov, S., McDonald, K. C., Marshall, J., Melton, J. R., Morino, I., O'Doherty, S.,
841 Parmentier, F. J. W., Patra, P. K., Peng, C., Peng, S., Peters, G. P., Pison, I., Prigent, C.,

842 Prinn, R., Ramonet, M., Riley, W. J., Saito, M., Schroeder, R., Simpson, I. J., Spahni, R.,
843 Steele, P., Takizawa, A., Thornton, B. F., Tian, H., Tohjima, Y., Viovy, N., Voulgarakis, A.,
844 van Weele, M., van der Werf, G., Weiss, R., Wiedinmyer, C., Wilton, D. J., Wiltshire, A.,
845 Worthy, D., Wunch, D. B., Xu, X., Yoshida, Y., Zhang, B., Zhang, Z., and Zhu, Q.: The
846 global methane budget: 2000-2012, *Earth System Science Data Discussion*, 2016, 1-79,
847 2016.

848 Saunio, M., Bousquet, P., Poulter, B., Peregón, A., Ciais, P., Canadell, J. G., Dlugokencky, E.
849 J., Etiope, G., Bastviken, D., Houweling, S., Janssens-Maenhout, G., Tubiello, F. N.,
850 Castaldi, S., Jackson, R. B., Alexe, M., Arora, V. K., Beerling, D. J., Bergamaschi, P., Blake,
851 D. R., Brailsford, G., Bruhwiler, L., Crevoisier, C., Crill, P., Covey, K., Frankenberg, C.,
852 Gedney, N., Höglund-Isaksson, L., Ishizawa, M., Ito, A., Joos, F., Kim, H.-S., Kleinen, T.,
853 Krummel, P., Lamarque, J. F., Langenfelds, R., Locatelli, R., Machida, T., Maksyutov, S.,
854 Melton, J. R., Morino, I., Naik, V., O'Doherty, S., Parmentier, F. J. W., Patra, P. K., Peng, C.,
855 Peng, S., Peters, G. P., Pison, I., Prinn, R., Ramonet, M., Riley, W. J., Saito, M., Santini, M.,
856 Schroeder, R., Simpson, I. J., Spahni, R., Takizawa, A., Thornton, B. F., Tian, H., Tohjima,
857 Y., Viovy, N., Voulgarakis, A., Weiss, R., Wilton, D. J., Wiltshire, A., Worthy, D., Wunch,
858 D., Xu, X., Yoshida, Y., Zhang, B., Zhang, Z., and Zhu, Q.: Variability and quasi-decadal
859 changes in the methane budget over the period 2000–2012, *Atmosphere Chemistry and*
860 *Physics*, 17, 11135-11161, 2017.

861 Schwietzke, S., Sherwood, O. A., Bruhwiler, L. M. P., Miller, J. B., Etiope, G., Dlugokencky, E.
862 J., Michel, S. E., Arling, V. A., Vaughn, B. H., White, J. W. C., and Tans, P. P.: Upward
863 revision of global fossil fuel methane emissions based on isotope database, *Nature*, 538, 88-
864 91, 2016.

865 Simpson, I. J., Sulbaek Andersen, M. P., Meinardi, S., Bruhwiler, L., Blake, N. J., Helmig, D.,
866 Rowland, F. S., and Blake, D. R.: Long-term decline of global atmospheric ethane
867 concentrations and implications for methane, *Nature*, 488, 490-494, 2012.

868 Smith, M. L., Kort, E. A., Karion, A., Sweeney, C., Herndon, S. C., and Yacovitch, T. I.:
869 Airborne ethane observations in the Barnett Shale: Quantification of ethane flux and
870 attribution of methane emissions, *Environmental Science & Technology*, 49, 8158-8166,
871 2015.

872 Sonnemann, G. R. and Grygalashvily, M.: Global annual methane emission rate derived from its
873 current atmospheric mixing ratio and estimated lifetime, *Annales Geophysicae*, 32, 277-283,
874 2014.

875 Sun, K., Tao, L., Miller, D. J., Khan, A. M., and Zondlo, M. A.: On-road ammonia emissions
876 characterized by mobile, open-path measurements, *Environmental Science & Technology*,
877 48, 3943-3950, 2014.

878 Tanaka, T., Yates, E., Iraci, L. T., Johnson, M. S., Gore, W., Tadi, J. M., Loewenstein, M., Kuze,
879 A., Frankenberg, C., Butz, A., and Yoshida, Y.: Two-year comparison of airborne
880 measurements of CO₂ and CH₄ with GOSAT at Railroad Valley,
881 Nevada, *IEEE Transactions on Geoscience and Remote Sensing*, 54, 4367-4375, 2016.

882 Thompson, D., Leifer, I., Bovensman, H., Eastwood, M., Fladeland, M., Frankenberg, C.,
883 Gerilowski, K., Green, R., Krautwurst, S., Krings, T., Luna, B., and Thorpe, A. K.: Real-time
884 remote detection and measurement for airborne imaging spectroscopy: A case study with
885 methane, *Atmospheric Measurement Techniques*, 8, 1-46, 2015.

886 VanCuren, R.: Transport aloft drives peak ozone in the Mojave Desert, *Atmospheric*
887 *Environment*, 109, 331-341, 2015.

888 Wennberg, P. O., Mui, W., Wunch, D., Kort, E. A., Blake, D. R., Atlas, E. L., Santoni, G. W.,
889 Wofsy, S. C., Diskin, G. S., Jeong, S., and Fischer, M. L.: On the sources of methane to the
890 Los Angeles atmosphere, *Environmental Science & Technology*, 46, 9282-9289, 2012.
891 White, W. H., Anderson, J. A., Blumenthal, D. L., Husar, R. B., Gillani, N. V., Husar, J. D., and
892 Wilson, W. E.: Formation and transport of secondary air pollutants: Ozone and aerosols in
893 the St. Louis urban plume, *Science*, 194, 187-189, 1976.
894 Wunch, D., Wennberg, P. O., Toon, G. C., Keppel-Aleks, G., and Yavin, Y. G.: Emissions of
895 greenhouse gases from a North American megacity, *Geophysical Research Letters*., 36, 2009.
896 Yacovitch, T. I., Herndon, S. C., Pétron, G., Kofler, J., Lyon, D., Zahniser, M. S., and Kolb, C.
897 E.: Mobile laboratory observations of methane emissions in the Barnett Shale Region,
898 *Environmental Science & Technology*, 49, 7889-7895, 2015.
899 Yates, E. L., Iraci, L. T., Roby, M. C., Pierce, R. B., Johnson, M. S., Reddy, P. J., Tadić, J. M.,
900 Loewenstein, M., and Gore, W.: Airborne observations and modeling of springtime
901 stratosphere-to-troposphere transport over California, *Atmospheric Chemistry Physics*, 13,
902 12481-12494, 2013.
903 Zhong, S., Whiteman, C. D., and Bian, X.: Diurnal evolution of three-dimensional wind and
904 temperature structure in California's Central Valley, *Journal of Applied Meteorology*, 43,
905 1679-1699, 2004.
906
907

908 **FIGURE CAPTIONS**

909 **Figure 1. (a)** Full surface and airborne data for 19 Aug. 2015 mapped over California topography. White
910 arrow shows Bakersfield. Data key on panel. **(b)** Study area map showing direction of daytime prevailing
911 winds and nearby mountain topography (Google Earth, 2016). See Supp. Fig. S1 for a high-altitude (20-
912 km) photo of the entire study area and surrounding terrain.

913
914 **Figure 2.** Study platforms. (a) AutoMOBILE trace Gas (AMOG) Surveyor, Kern River oil field in
915 background. Photo courtesy Ira Leifer. (b) The Alpha Jet Atmospheric eXperiment (AJAX) aircraft, photo
916 courtesy Akihiko Kuze, JAXA. See Supplemental Material Section 1 for further details.

917
918 **Figure 3.** (a) Pre-survey, upwind AMOG surface and AJAX airborne methane (CH_4) and winds for
919 vertical profile on the Delano – Alta Sierra transect (α – α'). Inset shows area map. (b) Post survey,
920 downwind AMOG surface profile ascent Edison-Breckenridge (ϵ – ϵ') and descent Breckenridge-Bodfish-
921 Caliente (τ – τ'). Upwind profile visible top left. Planetary boundary layer (PBL) identified.

922
923 **Figure 4.** Surface altitude (z) above mean sea level profiles for west-east Delano-Alta Sierra transect (Fig.
924 3A, α – α') for AMOG and AJAX (a) methane (CH_4), (b) carbon dioxide (CO_2), (c) ozone (O_3), (d)
925 temperature (T), and (e) relative humidity (RH). Also shown on (d) are the dry, average, and wet adiabatic
926 lapse rates. Data key on panel, planetary boundary layer (PBL), labeled. Green arrow shows extrapolation
927 of AJAX trend to Shirley Meadows altitude (2058 m).

928
929 **Figure 5.** Surface altitude (z) above sea level profiles for Edison-Breckenridge ascent (red) and descent
930 (blue) to Bodfish and then Caliente profile (magenta) (Fig. 3b) for AMOG Surveyor (a) methane (CH_4),
931 (b) carbon dioxide (CO_2), (c) relative humidity (RH), (d) temperature (T), north wind (U_{north}), for (e)
932 ascent and (f) descent, dots shown 50-m altitude binned averaged, and (g) ozone (O_3). Planetary
933 Boundary Layer (PBL) labeled.

934
935 **Figure 6.** Altitude (z) profiles for (a) west (upslope) and (b) north (cross slope) wind components from
936 AMOG and AJAX for overlapping altitudes of the Delano–Alta Sierra transit (Fig. 3, α – α'), 100-m
937 altitude rolling-averaged data for AJAX, AMOG, and AMOG upper 5% of winds. Data key on figure.

938

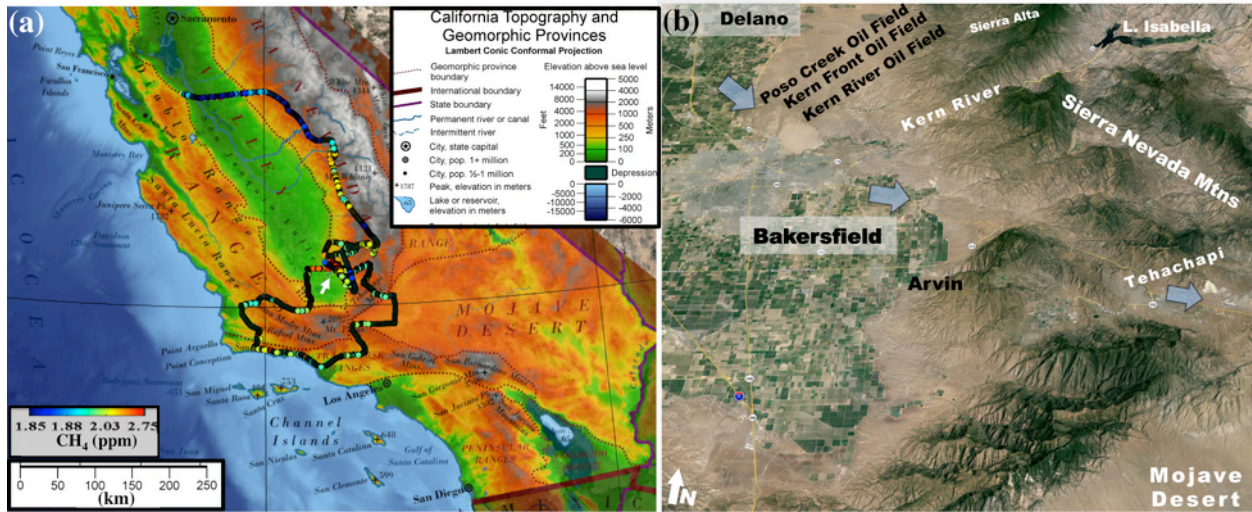
939 **Figure 7.** Combined AJAX and AMOG winds and *in situ* (a) methane (CH₄) and (b) carbon dioxide
940 (CO₂) for the Kern Fields on 19 Aug. 2015 for prevailing wind conditions. White arrow to the west of
941 Kern Front oil field shows location of nearby dairy. Greek letters identify two downwind curtains. Red
942 star on (b) locates origin for transect $\gamma-\gamma'$. Data keys on figure.

943
944 **Figure 8.** (a) Methane (CH₄) altitude (z) profiles for 19 Aug. 2015 for AJAX (black) and AMOG (gray)
945 data. (b) Interpolated, fused AJAX and AMOG CH₄ data, with respect to lateral east distance (x) relative
946 to 119.0023°W, 35.3842°N for data plane $\gamma-\gamma'$ (Fig. 7). Dashed lines show data locations. (c) CH₄
947 anomaly (CH₄') relative to the background data plane (Supp. Fig. S6A). (d) Vertical normal wind profile
948 (U_n) from AJAX (black) and AMOG (gray) data during ascent/descent, (e) interpolated, fused U_n , and (f)
949 CH₄ flux (Q_{CH_4}) for the Kern Fields. Data key on panels.

950
951 **Figure 9.** (a) Vertical carbon dioxide (CO₂) altitude (z) profile data for 19 Aug. 2015 for AJAX (black)
952 and AMOG (gray) data. (b) Interpolated, fused AJAX and AMOG CO₂ data curtain with respect to lateral
953 east distance, x , relative to 119.0023°W, 35.3842°N for curtain $\gamma-\gamma'$ (Fig. 7b). Dashed lines show data
954 locations. (c) CO₂ anomaly (CO₂'). (d) Vertical normal wind profile (U_n). (e) Interpolated, fused U_n , and
955 (f) CO₂ flux (Q_{CO_2}) for the Kern River and Kern Front oil fields for 19 Aug. 2015. Data key on panels.

956
957

958 Fig. 1

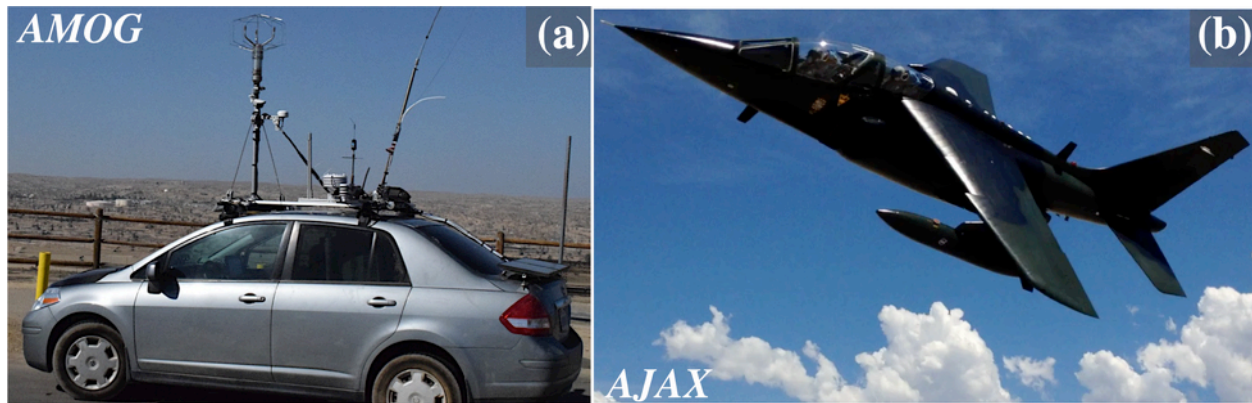


959

960

961

962 Fig. 2

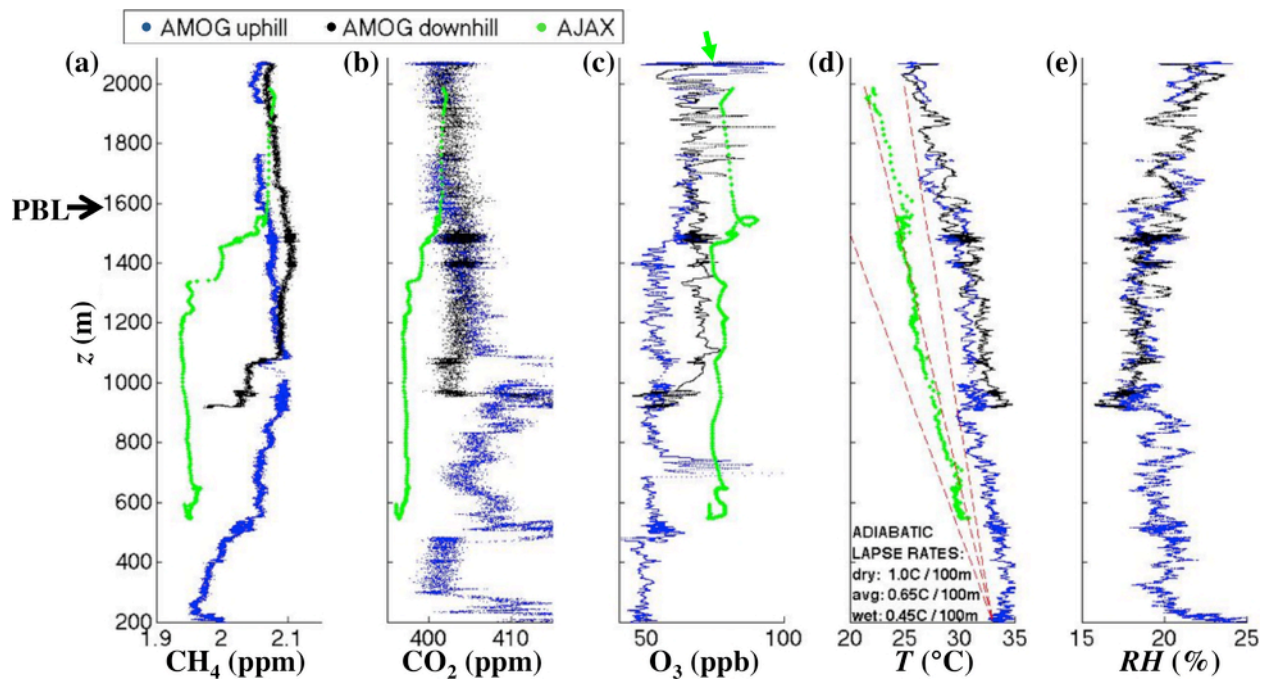


963

964

965

970 Fig. 4

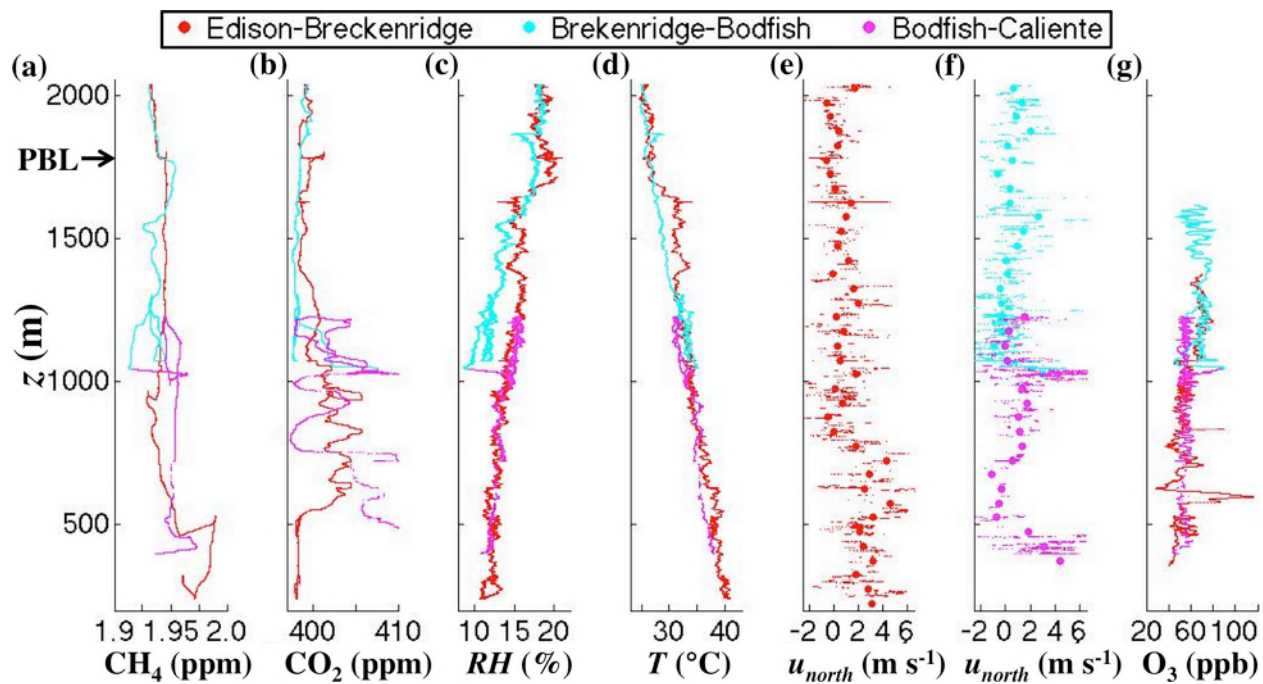


971

972

973

974 Fig. 5

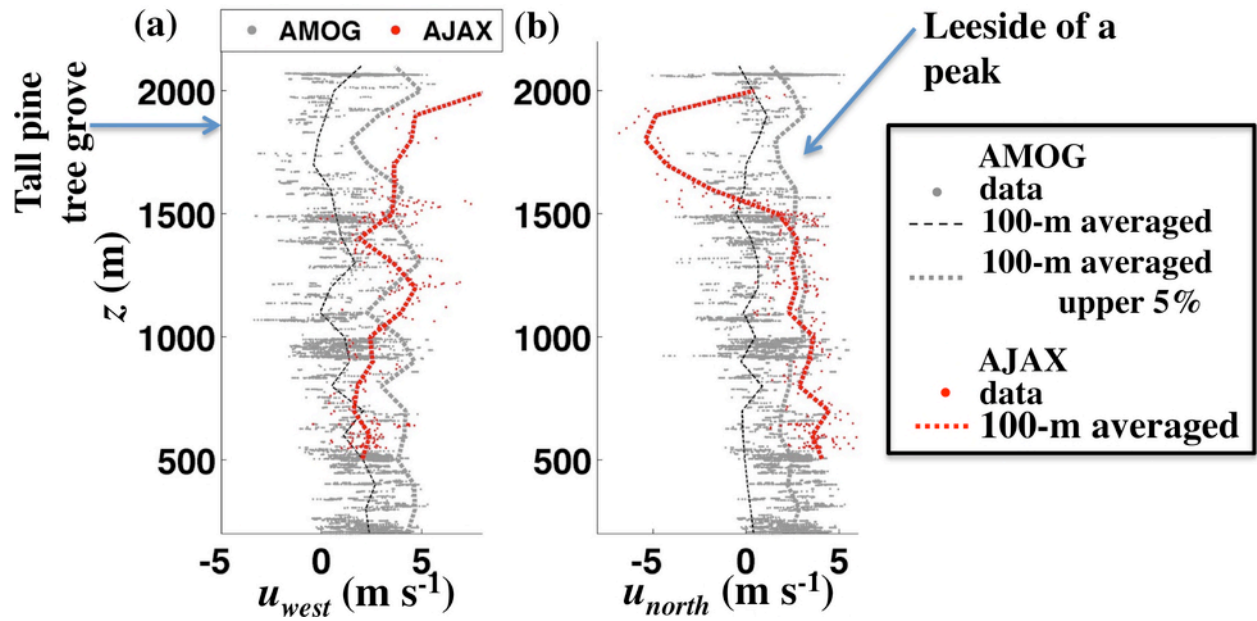


975

976

977

978 Fig. 6

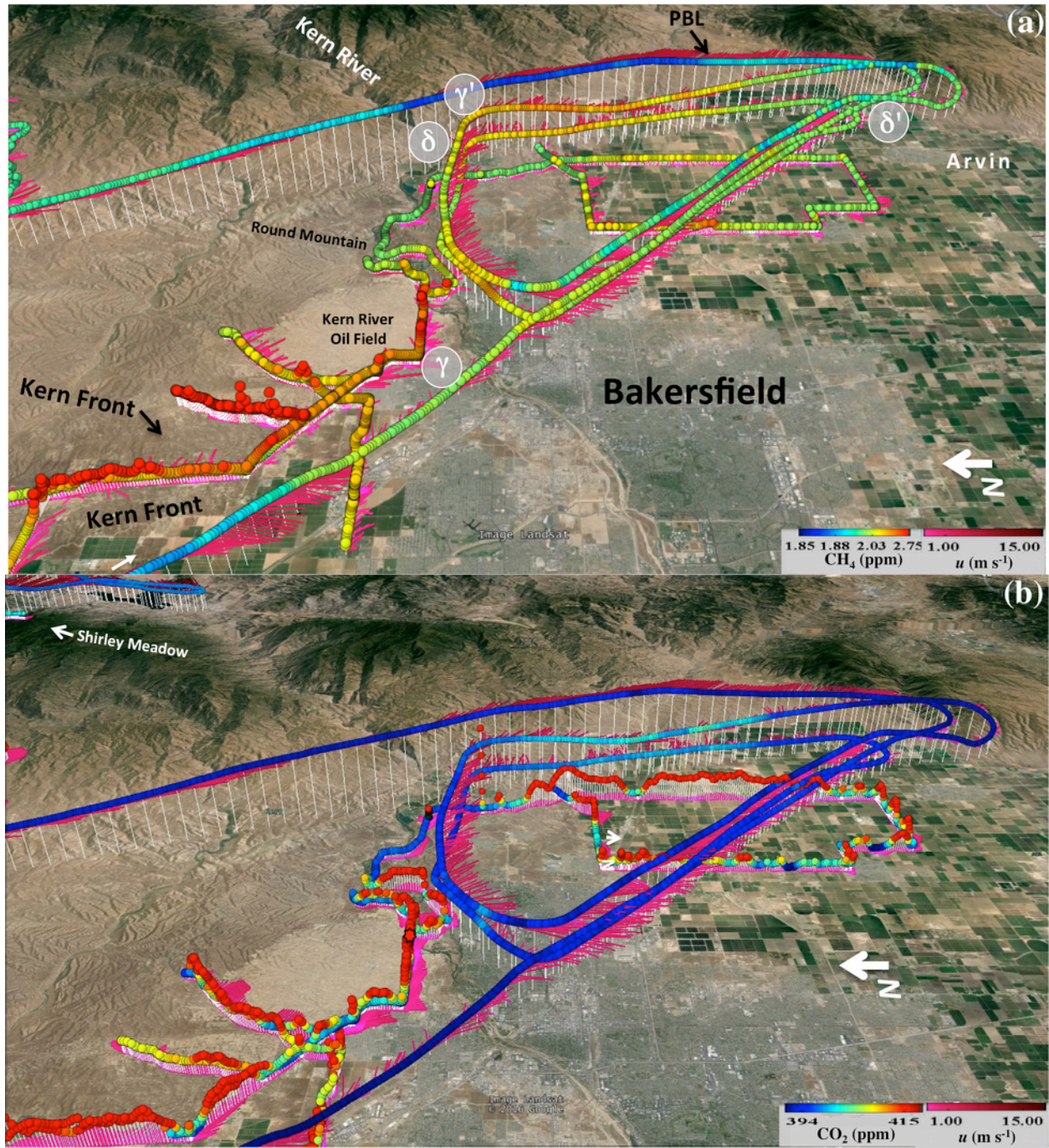


979

980

981

982 Fig. 7

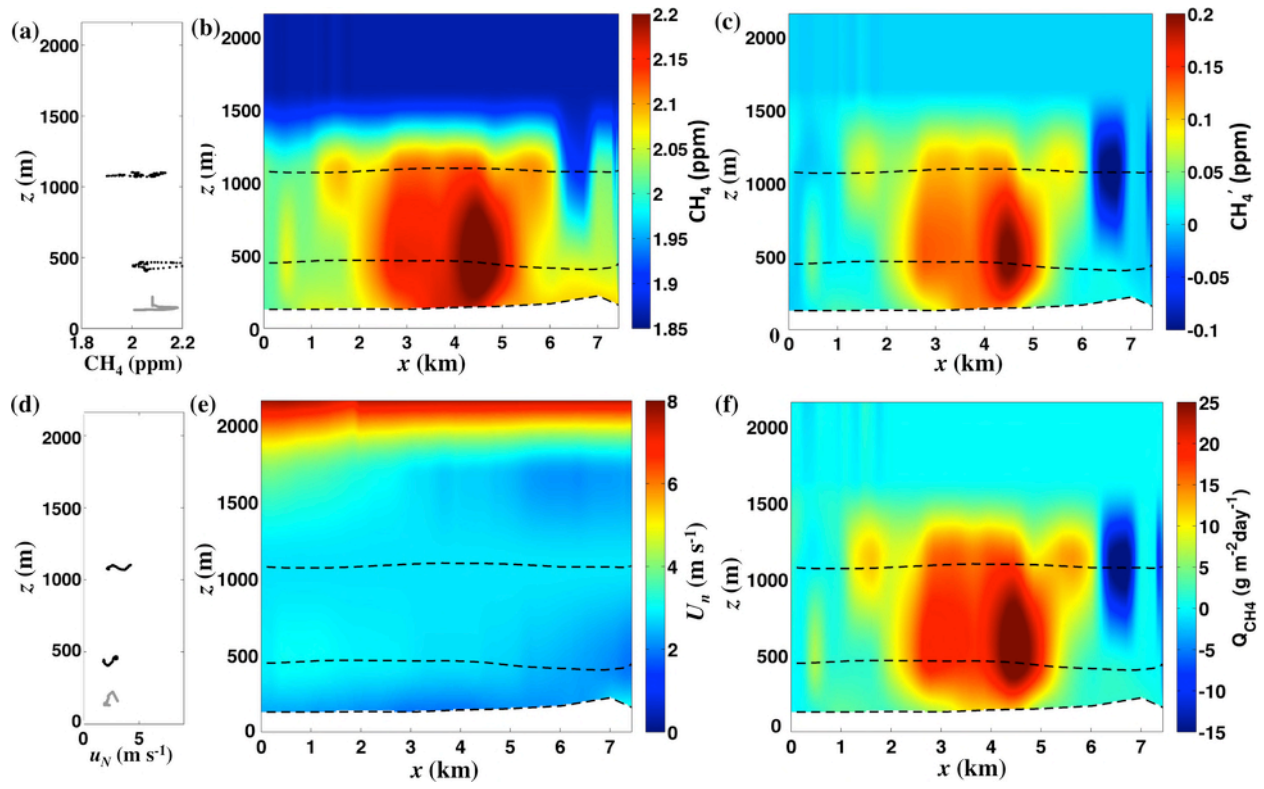


983

984

985

986 Fig. 8

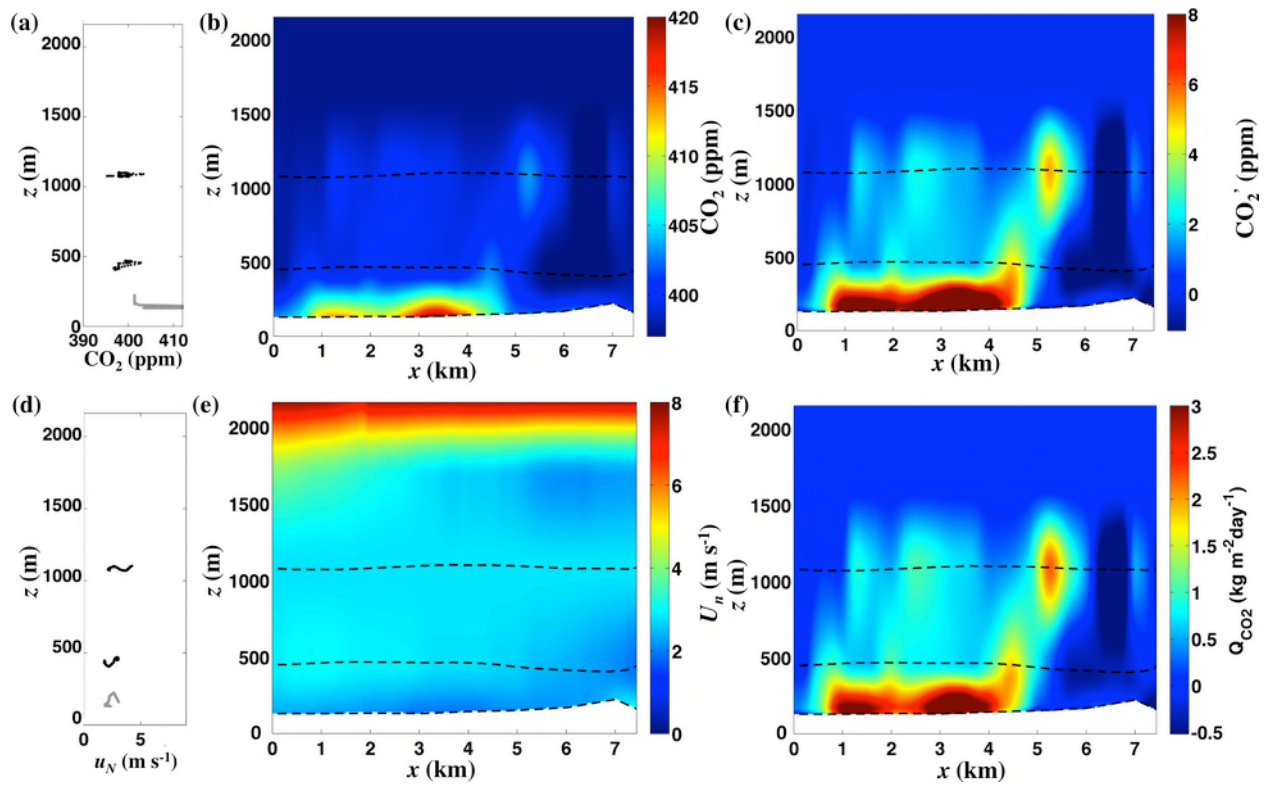


987

988

989

990 Fig. 9



991